Bulletin of the Seismological Society of America, Vol. XX, No. XX, pp. –, – 2019, doi: 10.1785/0120190017

Ⓔ

Injection-Induced Seismicity and Fault-Slip Potential in the Fort Worth Basin, Texas

by Peter H. Hennings, Jens-Erik Lund Snee, Johnathon L. Osmond,* Heather R. DeShon, Robin Dommisse, Elizabeth Horne, Casee Lemons, and Mark D. Zoback

Abstract The rate of seismicity in the hydrocarbon-producing Fort Worth Basin of north-central Texas, which underlies the Dallas–Fort Worth metropolitan area, increased markedly from 2008 through 2015, coinciding spatiotemporally with injection of 2 billion barrels of wastewater into deep aquifers. Although the rate of seismicity has declined with injection rates, some earthquake sequences remained active in 2018 and new clusters have developed. Most of this seismicity occurred away from regionally mapped faults, challenging efforts to constrain the continuing hazards of injection-induced seismicity in the basin. Here, we present detailed new models of potentially seismogenic faults and the stress field, which we use to build a probabilistic assessment of fault-slip potential. Our new fault map, based on reflection seismic data, tens of thousands of well logs, and outcrop characterization, includes 251 basement-rooted normal faults that strike dominantly north-northeast, several of which extend under populated areas. The updated stress map indicates a relatively consistent north-northeast–south-southwest azimuth of the maximum horizontal principal stress over seismically active parts of the basin, with a transition from strike-slip faulting in the north to normal faulting in the southeast. Based on these new data, our probabilistic analysis shows that a majority of the total trace length of the mapped faults have slip potential that is equal to or higher than that of the faults that have already hosted injection-induced earthquake sequences. We conclude that most faults in the system are highly sensitive to reactivation, and we postulate that many faults are still unidentified. Ongoing injection operations in the region should be conducted with these understandings in mind.

Supplemental Content: Tabulation of data used for the interpretation of $S_{H\,max}$ in the Fort Worth basin.

Introduction

The Fort Worth basin (FWB) underlies a broad area of north-central Texas (Figs. 1 and 2), including most of the Dallas–Fort Worth (DFW) metropolitan area. The FWB hosts conventional and unconventional hydrocarbon-producing intervals including the Mississippian Barnett Shale (Pollastro *et al.*, 2007). Like many areas of the south-central United States, the FWB experienced a sharp increase in earthquakes over the last 10 yr that has been linked to the disposal of oilfield wastewater into deep wells, with most disposal targeting the carbonate-rich Ordovician Ellenburger Group (Ellsworth, 2013; Weingarten *et al.*, 2015). This process is called saltwater disposal (SWD). Only two earthquakes were recorded in the basin between 1970 and 2007, but 18 $M_w \geq 2.5$ events were cataloged in 2008 through 2010, 101 from 2011 through 2015, and 6 since 2015 (U.S. Geological Survey [USGS] Advanced National Seismic System Comprehensive Catalog [ComCat], see Data and Resources). The largest earthquake was an M_w 4.0 event that occurred in Johnson County near Venus in 2015. The rate of SWD in the basin increased considerably beginning in 2005 and peaked at 28 MMbbl/month in late 2011, but the largest number of earthquakes per month occurred in late 2013 (Fig. 3). Months with large numbers of earthquakes continued to occur throughout 2014 and 2015 although the average monthly rate of SWD in the basin decreased by 43% during that time. This trend of a marked increase and decrease in seismicity with a time delay following an increase and decrease in the rate of SWD roughly mirrors the behavior

*Also at Centre for Earth Evolution and Dynamics (CEED), P.O. Box 1028 Blindern, NO-0315 Oslo, Norway.

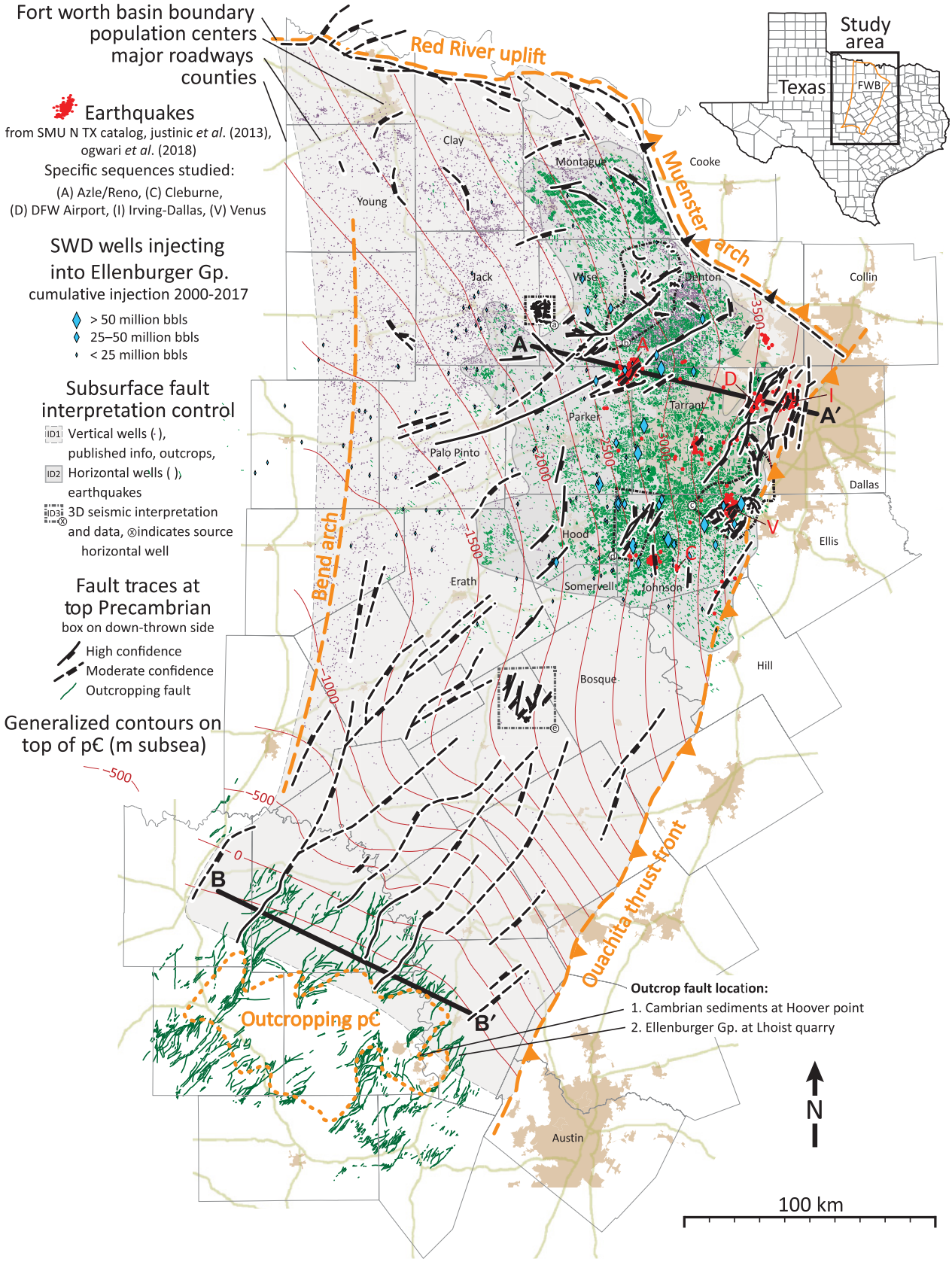

Figure 1. Map showing the study area in north-central Texas, the traces of basement-rooted faults in our interpretation, and other data used in our analysis. The faults originated in a 3D structural model and the traces shown map the intersection of the 3D faults with the unconformity between Precambrian (pЄ) igneous and metamorphic rocks and overlying Phanerozoic sedimentary rocks.

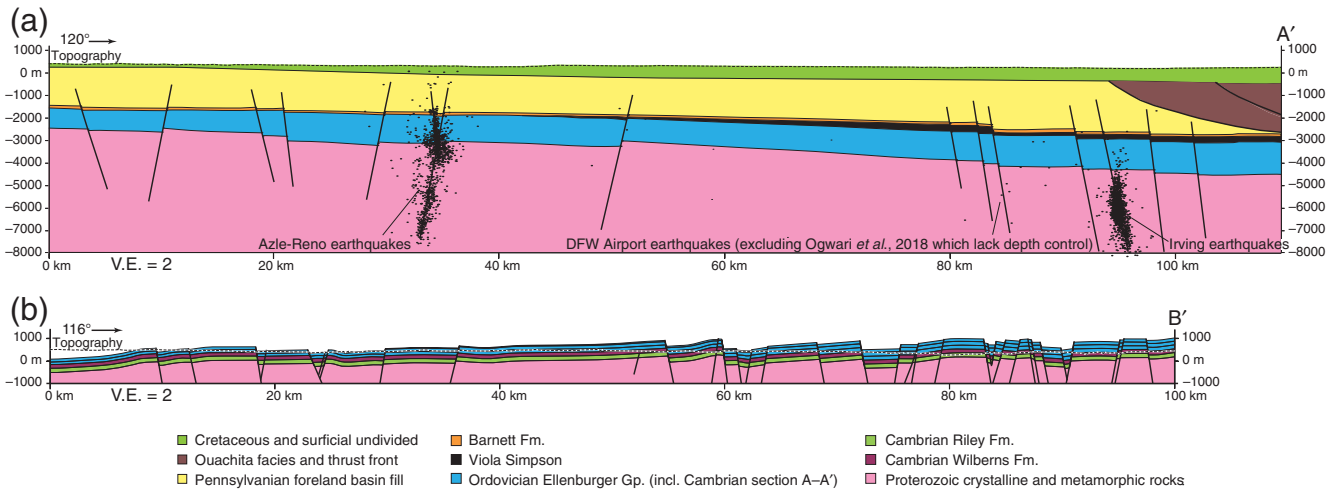

Figure 2. Cross-section traces (a) A–A′ (though the center of the basin) and (b) B–B′ (through the outcropping domain) illustrate the general structural style and spatial variability of basement-rooted normal faults. Cross section A–A′ shows recent earthquakes projected into the line of section from nearby sequences (Fig. 1). V.E., vertical exaggeration.

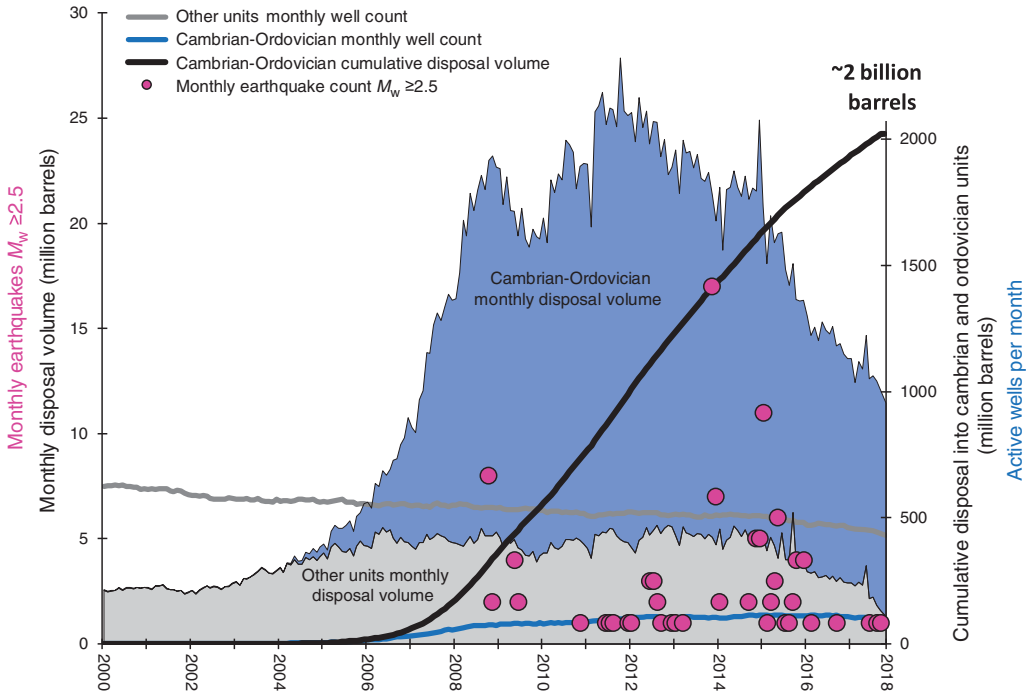

Figure 3. Monthly saltwater disposal into the Fort Worth basin showing supra-Barnett Shale disposal intervals in gray, sub-Barnett Shale disposal intervals in blue, the number of active disposal wells, the cumulative injection, and the monthly count of $M_w \geq 2.5$ earthquakes from Advanced National Seismic System Comprehensive Catalog between January 2002 and December 2017.

described by Langenbruch and Zoback (2016) for seismicity due to SWD into the stratigraphically equivalent Arbuckle Group in central and northern Oklahoma. The time delay for the onset and later decline of seismicity in the FWB was several years, whereas the time delay in northern Oklahoma was approximately 1 yr. The peak monthly rate of SWD in northern Oklahoma was roughly three times that of the FWB, and the resulting earthquake rate and maximum magnitude were considerably higher.

Assessing the distribution and orientation and of faults relative to the stress field is critical for characterizing the hazard of fault reactivation and managing induced seismicity (Zoback, 2012; Ellsworth, 2013; Underground Injection Control National Technical Workgroup, 2015; Huang *et al.*, 2017). However, like in Oklahoma and the Permian basin of west Texas and southeast New Mexico (Walsh and Zoback, 2016; Lund Snee and Zoback, 2018), existing fault maps in the FWB are coarse in resolution and several decades old,

challenging efforts to constrain the ongoing seismic hazard and to understand the architecture of the basin and region. The most recent basinwide interpretation of faults was conducted as part of a study of the entire state and lacked both dip and depth information (Ewing, 1991). To improve the understanding of seismic hazard in the FWB, we present below a much more detailed interpretation that includes 251 faults. We also present an updated stress map, which we use together with the fault model to probabilistically estimate fault-slip potential (FSP) using two scenarios. The results are maps of FSP associated with the mapped faults for the entire FWB and for more local scales where the earthquake sequences occurred. The two FSP scenarios include (1) a hydrostatic case representing the conditions prior to the onset of earthquakes and (2) a plausible increase in pore fluid pressure that can be used to assess the general hazard of SWD. We compare the two FSP cases to investigate how the fault reactivation hazard caused by SWD may have increased in the FWB, and we apply the results to the faults that have locally hosted significant earthquake sequences to qualitatively scale FSP to highlight how sensitive the basinwide population of faults—both interpreted and still unknown—may be.

Seismotectonic Setting

Earthquakes in the FWB occur primarily in discrete spatial clusters (Quinones *et al.*, 2019), mostly on previously unmapped faults (Fig. 1). Five named earthquake sequences have been studied using local seismic network data: the 2008–2009 DFW airport (Frohlich *et al.*, 2010, 2011, 2016; Janská and Eisner, 2012; Reiter *et al.*, 2012; Ogwari *et al.*, 2018), the 2009 Cleburne (Howe, 2012; Justinic *et al.*, 2013), the 2013–2014 Azle–Reno (Hornbach *et al.*, 2015), the 2015–2017 Irving–Dallas (Frohlich *et al.*, 2010, 2011; Magnani *et al.*, 2017; Ogwari *et al.*, 2018), and the 2015 M_w 4.0 Venus (Scales *et al.*, 2017). Most earthquakes produce normal-faulting mechanisms associated with northeast-striking faults (Magnani *et al.*, 2017). Detailed studies indicate that many of the sequences began prior to the first felt events and/or generated small-magnitude earthquakes well past the original felt earthquakes (Reiter *et al.*, 2012; Magnani *et al.*, 2017). The multiple $M_w \geq 3.5$ Azle–Reno earthquakes and the Irving–Dallas doublet of M_w 3.5 and M_w 3.6 in January 2015 refocused attention on understanding the hazard associated with earthquakes in the FWB. Local and regional seismic networks have routinely reported data for the basin since December 2013 to supplement the USGS catalog (DeShon *et al.*, 2018; the Texas Seismologic Network [TexNet] earthquake catalog). Many of the earthquake sequences listed generated seismicity through 2018, and several new clusters have developed in recent years (DeShon *et al.*, 2018).

The vast majority of earthquakes recorded in the FWB in recent years occurred beneath the sedimentary succession, in Proterozoic crystalline basement (Frohlich *et al.*, 2011; Hornbach *et al.*, 2015; Magnani *et al.*, 2017; Scales *et al.*, 2017; Quinones *et al.*, 2018). Of the well-studied sequences, only the Azle–Reno sequence extended into the sedimentary overburden (Hornbach *et al.*, 2015; Fig. 2). The consensus of published work suggests that the most likely mechanism of induced fault reactivation in areas experiencing appreciable SWD is reduction in fault-normal stress due to increases of pore pressure in sedimentary injection intervals that are in hydrogeologic continuity with faults in the basement on local to regional scales (Zhang *et al.*, 2013; Gono *et al.*, 2015; Walsh and Zoback, 2015; Hornbach *et al.*, 2016). Therefore, we focused on identifying faults that are evident in the sedimentary realm and root into the Precambrian basement.

Our work here focusses on the FWB proper—the 56,000 km^2 region east of the Bend Arch. The fault structure of the FWB is relatively well known within the petroleum industry but little information on subsurface faults is in the public domain due to the proprietary nature of the data. The basin is bounded on the southeast by the northwest-vergent Ouachita fold and thrust belt, and on the north by high-angle reverse faults that follow the southwestern margins of the Muenster and Red River arches. These bounding structures grew during development of the FWB in the foreland of the Ouachita orogenic belt, which encroached northwestward over the basin in late Mississippian through Pennsylvanian time (Flawn *et al.*, 1961; Ewing, 1991; Poole *et al.*, 2005; Pollastro *et al.*, 2007; George, 2016; Leary *et al.*, 2017; Magnani *et al.*, 2017). Within the basin, major faults that cut the sedimentary succession have linear map traces, display normal-sense offset, and strike dominantly northeast. Many of these normal faults are rooted in the Precambrian crystalline basement, and this episode of faulting has been attributed to basin subsidence and flexure produced by loading along the southeastern margin when the basin was tectonically overridden (Walper, 1982; Viele and Thomas, 1989; Alsalem *et al.*, 2017). Throughout the basin, the tips of these normal faults typically do not extend above the unconformity separating Pennsylvanian and Cretaceous rocks, suggesting that they experienced little normal-sense slip since they formed in Late Paleozoic time (Magnani *et al.*, 2017). Because the FWB developed on the margin of the Laurentian continent produced by late Proterozoic and Cambrian rifting (Walper, 1982; Thomas, 2004), it is likely that the location and character of these basement-rooted faults is, at least in part, governed by inheritance from a pre-existing, regionally developed fabric. The northeast trend of the rift margin is roughly parallel to the trend of the FWB axis, the strike of the Ouachita thrust front, and the dominant strike of the faults that we characterize here (Fig. 1). In addition, there are faults within the sedimentary succession that have concentric strike orientations and are generally smaller (mostly <2 km strike length) that originated from collapse of karst features within the carbonate-rich Ordovician Ellenburger Group (Hardage *et al.*, 1996; Sullivan *et al.*, 2006; McDonnell *et al.*, 2007). No published work has definitively linked observed seismicity to faults of exclusively karst-related origin in the FWB.

Fault Interpretation Method and Results

As with any interpretation lacking direct physical observation, models of subsurface structure will differ somewhat depending on the interpreter; the quantity, quality, and spatial extent of available control data; the manner in which data are weighted; and the interpretation procedures employed. To build our interpretation, we considered a wide array of existing and new control information: seismic reflection data provided by petroleum operators, regional subsurface mapping, new outcrop mapping, earthquake hypocenters and focal plane mechanisms, and all publicly available information sources. We integrated these data into a geological model in which we interactively evaluated all new and existing control information and interpreted faults in 3D following methodology outlined by Krantz and Neely (2016).

Based on the amount, quality, and strength of information controlling the interpretation, we classify the faults according to levels of confidence. Our criteria for faults of high confidence is that there is sufficient and detailed spatial and depth control at the ∼0–5 km scale to detect the presence of a fault and to interpret their lateral extent, dip direction, degree of segmentation, and magnitude of offset. Data types that yield high-confidence fault interpretations include 3D seismic reflection surveys, tightly spaced horizontal wells, earthquake clusters that form subplanar 3D geometries as cataloged by local dense monitoring arrays using high-resolution velocity models, outcrop maps, and observations. In essence, faults with a high level of confidence have supporting data that make their occurrence a strong likelihood as mapped. Our criteria for faults of moderate confidence include sufficient spatial control at the ∼5 + km scale confirming the general presence and dip direction of a significant fault or fault system. Data types yielding moderate-confidence faults include horizon mapping using vertical wells, published interpretations using 2D reflection seismic data and vertical wells, direct projection from outcrop mapping, and maps and cross sections made public by the Texas Railroad Commission that were developed using comprehensive interpretation methods and data. Interpretation of the precise location, lateral extent, and degree of segmentation for these moderate-confidence faults is not possible given these types of control data. Faults with a moderate level of confidence have ample evidence to be included in the map, but there is uncertainty in their extent and continuity. Finally, faults with a low level of confidence lack sufficient evidence within our interpretation to warrant inclusion. There are numerous cases where our analysis provides additional constraints that alter the interpretations of faults from published studies. Many faults from Ewing (1991) are in this category, as are the faults in northeastern Johnson County interpreted by Magnani *et al.* (2017). We formulated the above confidence criteria such that a qualified interpreter using established methods and the same data would likely produce the same general interpretations. We delineate the types of data used to support the interpretation using aerial domains labeled ID1–3 as shown in Figure 1 and Table 1. Details of the methods and data used to interpret faults in the three areas are described next.

In the light gray region (ID1) that covers most (74%) of the study region in Figure 1, we newly interpreted and verified or modified faults identified by Belforte (1971), Thompson (1982), Ewing (1991), Hentz *et al.* (2012), and Eastman and Murin (2016). Control on the depths of stratigraphic markers such as the Barnett Shale, Ellenburger Group, and others are constrained by ∼12,500 vertical wells from the Bend Arch in the west to the Ouachita thrust in the east. Projecting from outcrop exposure of the southwest flank of the FWB in central Texas provides additional control for the locations and geometries of these faults (Kier *et al.*, 1976; Barnes and Rose, 1981; Ewing, 1991). Fault interpretations presented in Texas Railroad Commission hearing Docket 09-0296411 provide further control on faults in northeast Tarrant and northwest Dallas counties. Earthquake hypocenter data for the Irving–Dallas earthquake sequence provide constraints for northwest Dallas County. With the exception of faults interpreted from outcrops for which have high confidence, we characterize all other faults within ID1 as having moderate confidence. Within the zone labeled ID2 (covering 22% of the study area), we additionally include analysis of the trajectories of ∼21,000 horizontal wells within the core of the Barnett Shale production area to develop trend surfaces from which faults were interpreted (Fig. 4). Earthquake hypocenter data provided excellent constraints for interpreting faults associated with the Azle–Reno, DFW airport, Cleburne, and other unnamed sequences. Within the five small areas labeled ID3 in Figure 1 (4% of the study area), our interpretation was further constrained by information from 2D and 3D reflection seismic data, both previously published and newly available for this study. Such interpretations from reflection seismic datasets offer the greatest subsurface interpretation completeness and finest-scale control (McDonnell *et al.*, 2007; Elebiju *et al.*, 2010; Patterson, 2010; Khatiwada *et al.*, 2013). An example of our interpretation procedure using 3D seismic reflection data for faults in northeast Johnson County within the ID3c area is shown in Figure 5, and earthquake hypocenter locations for the Venus sequence further assisted with fault interpretation in ID3c. Area ID3c also provides an example of tectonic and karst-related faults existing in the same location, as described by McDonnell *et al.* (2007).

Our new interpretation has 251 faults with a cumulative trace length (CTL) of 2938 km that, with the exception of many relatively small faults in ID3a, are interpreted to root into the crystalline basement, extend upward into the Paleozoic succession, and range in trace length from 0.25 to 136 km (Figs. 1 and 6). The CTL of the 178 high-confidence faults is 1014 km, and it is 1924 km for the 73 moderate-confidence faults. The interpreted faults strike dominantly northeast and most dip steeply southeast. Based on the analysis presented in Figure 6, we conclude that within the ID3 areas we identified the majority of faults with

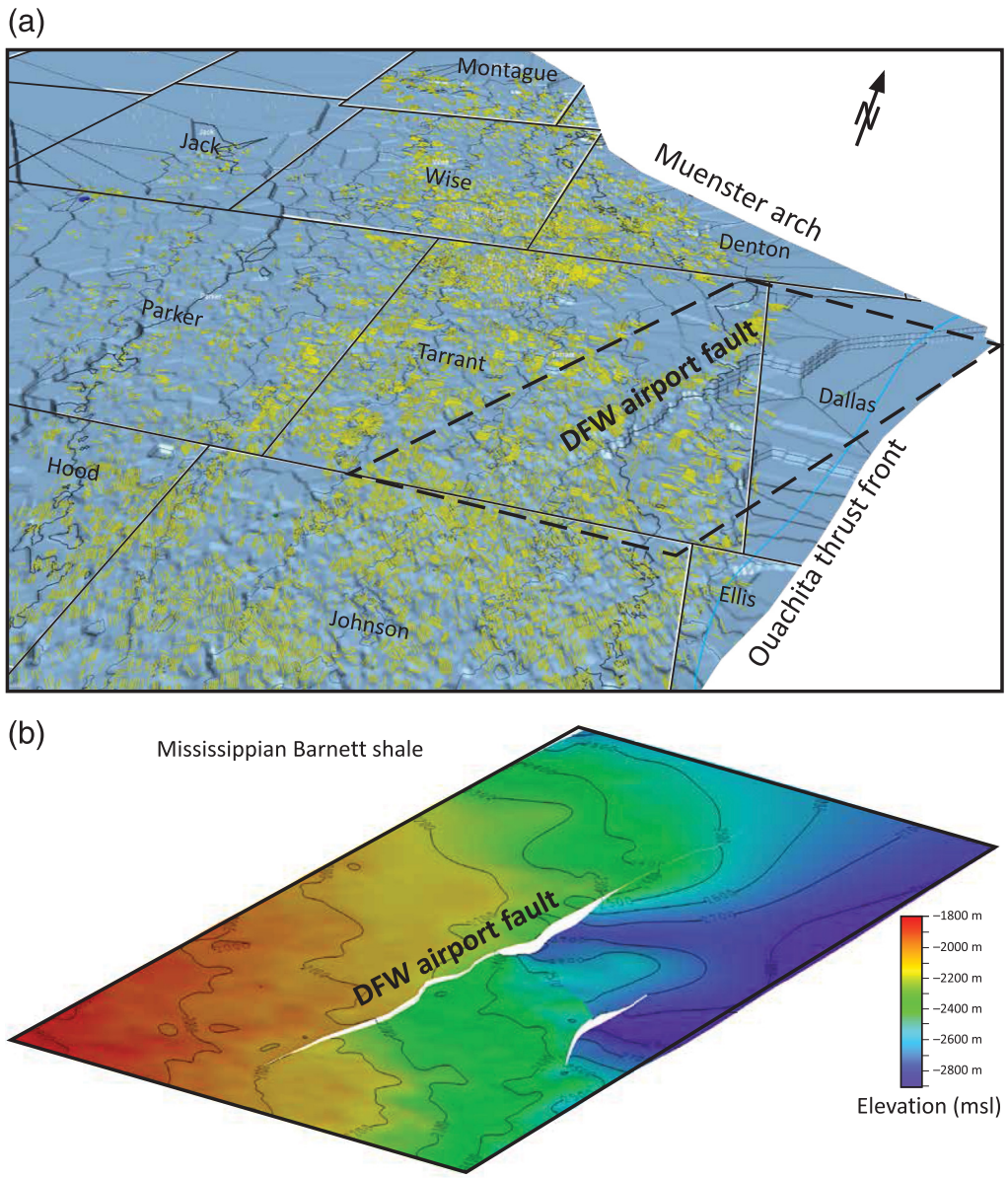

Figure 4. (a) Oblique view north-northwest illustrating how horizon surfaces were created using the horizontal legs of more than 21,000 horizontal wells (yellow shades) in the Mississippian Barnett Shale in the core production area of the basin. These horizon interpretations were used to map faults in the ID2 area of Figure 1. (b) Map showing detail of the Dallas–Fort Worth (DFW) airport fault, which has the largest maximum offset of any fault in the interpretation (~300 + m).

trace lengths greater than ~0.5 km that offset the Paleozoic sedimentary succession. Within areas ID1 and ID2, we estimate that we interpreted the majority of faults with trace lengths greater than ~5 km. This is not to say that we identified every potentially seismogenic fault in the FWB; a comparison of earthquake catalogs from Frohlich (2012), USGS ComCat, North Texas earthquake study (NTXES, Quinones *et al.*, 2019), and TexNet (Savvaidis *et al.*, 2019) show areas with a small number of low-magnitude unfelt earthquakes not associated with faults in our analysis. With the exception of the DFW airport fault, which is ~35 km long, it is striking that the other faults that hosted earthquakes are all less than 8 km long, underscoring the necessity of such detailed interpretations for studies of induced seismic hazards. All fault length data presented here, especially outside the ID3 interpretation areas, should be considered minimums due to the challenges of identifying fine-scale lateral fault tips using subsurface data. In addition, fault interpretations in areas with sparse control data such as parts of the ID1 area may inherently fail to characterize the existence and role of fault segmentation.

We make use of our new fault interpretation to estimate the FSP. For the FSP analysis, we extract fault segments at the intersection lines between the fault planes and the sediment-basement contact, employing a sampling length of 100 m (FSP samples). We chose to conduct our analysis at the depth of the sediment-basement contact because, as

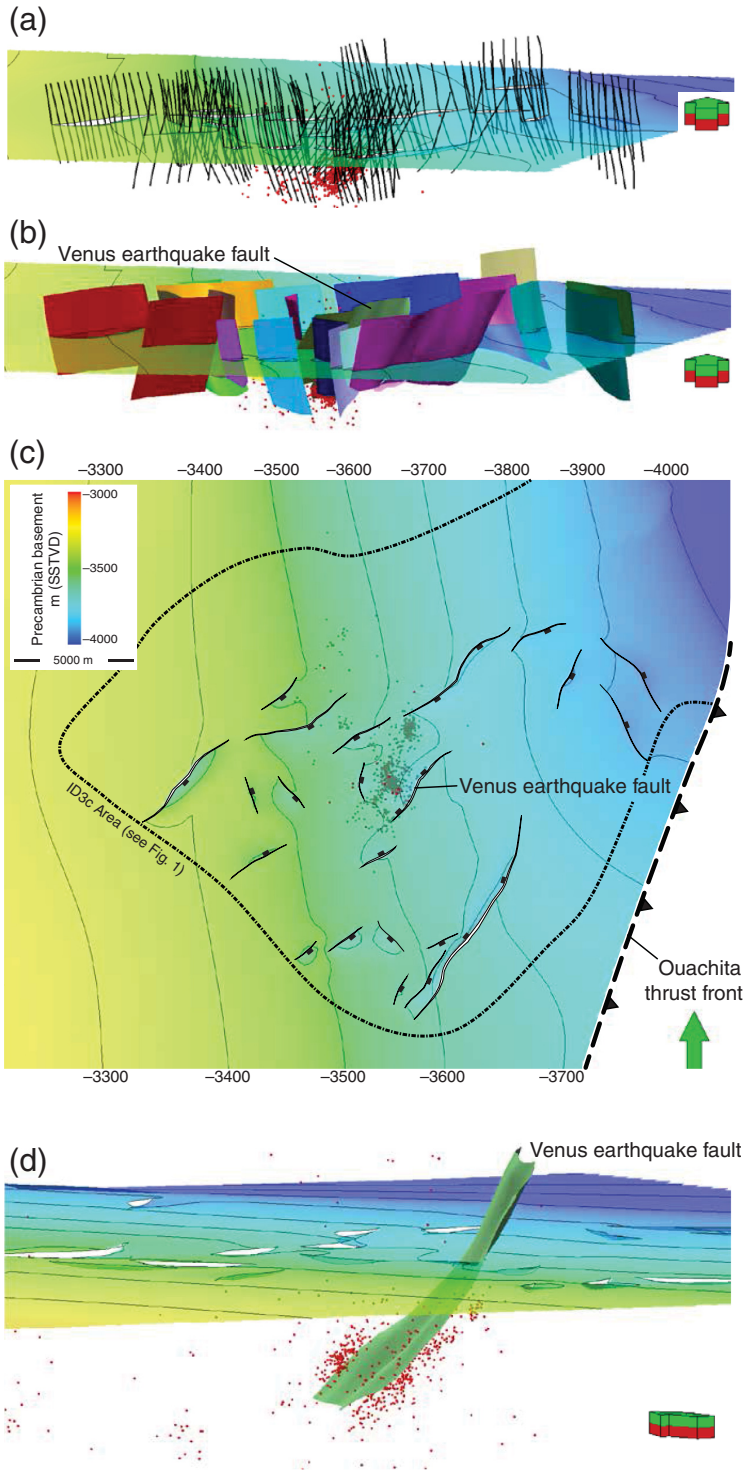

Figure 5. Method of fault interpretation from proprietary 3D reflection seismic data using the ID3c interpretation area in Johnson County as example. (a) Oblique view north of the faulted basement-sediment interface and fault lines interpreted from depth-converted vertical seismic profiles that sample the faults at multiple azimuths. Red dots are hypocenters from the Venus earthquake sequence. (b) Same view as (a) with 3D fault surfaces created from the fault lines. The upward tips of the faults are generally evident in the seismic data but the lower tips within basement, with the exception of the earthquake hypocenters, are unconstrained. (c) Map view of the faults with heaves (fault gaps) illustrated. (d) Oblique view northeast of the fault that is interpreted to have hosted the Venus earthquake sequence illustrating how the fault surface was interpreted with the earthquake hypocenters as additional control. SSTVD, total vertical depth below sea level.

described earlier, injection occurs above this level in the Ellenburger Group and the earthquakes dominantly occur below it, within the crystalline basement. Although fault strikes are generally well constrained in our analysis, fault dips are less certain. We estimated permissible dip ranges for faults lacking precise constraints by extracting average values from several fault populations that do have reliable dip information. Earthquake hypocenters clearly define the planes for five of our faults, yielding a mean dip of 67.8° (three faults in the Azle sequence area, the fault that hosted the Irving–Dallas events, and the Venus fault; Figs. 1, 3b, and 5d). Faults interpreted directly from 3D reflection seismic data (107 faults, all within ID3 areas in Fig. 1) yield a mean dip of 71.7°. Analysis of USGS geologic maps and our own fieldwork on the southwest flank of the FWB provides additional dip constraints for 14 mapped faults (mean dip = 72.9°). Small (outcrop scale) normal faults exposed in road cuts of Cambrian sediments at outcrop fault location 1 (Fig. 1) have a mean dip of 72.0° (267 smaller faults that are not included in our fault model). Small normal faults in quarry walls of Ordovician Ellenburger Group carbonate rocks at outcrop fault location 2 have a mean dip of 72.6° (1149 faults not included in the model). Based on the above data, we applied a dip of 72° to faults lacking definitive constraints, and we conservatively applied ±10° fault-dip uncertainty for the FSP analysis.

Stress Interpretation Method and Results

To more tightly constrain the stresses resolved on faults across the basin for FSP analysis, we collected 34 new and incorporated 47 previously published $S_{H\,max}$ orientations (listed in Ⓔ Dataset S1, available in the supplemental content to this article), and we improved the previous map of relative principal stress magnitudes (faulting regime) by Lund Snee and Zoback (2016). Here, we provide the methods used for data collection, and we describe the mapped stress field. Quality ratings were assigned on a scale from A (best) to D (unreliable), using updated criteria from Lund Snee and Zoback (2018) based on those established

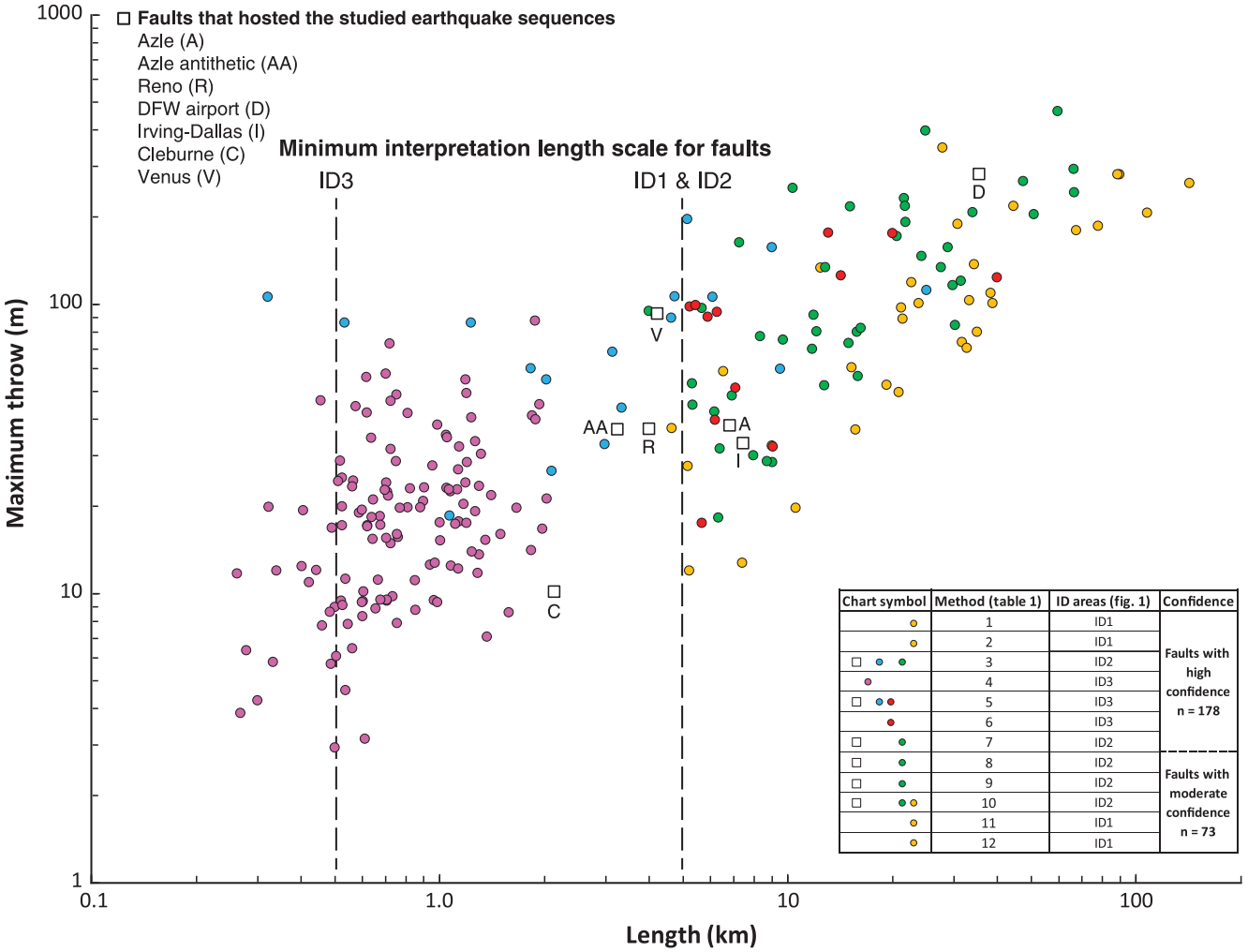

Figure 6. Fault trace length versus maximum throw for faults with reliable fault throw information. Data point colors represent different fault families based on location and control data used. The plot is also used to determine the minimum fault length scale associated with each fault interpretation technique and data type listed in Table 1.

Table 1

Data and Methods Used in the Fault Interpretation, Confidence Level Assigned to Types of Data and Methods, and the Interpretation Domains (ID1–3) Illustrated in Figure 1

	Fault Interpretation Data and Method Used	ID Areas (Fig. 2)	Confidence
1	Outcrop interpretation by the authors	ID1	Faults with high confidence (n = 178)
2	Published outcrop interpretation	ID1	
3	Earthquakes from dense monitoring arrays located with detailed velocity models	ID2	
4	Firsthand interpretation of 3D seismic data by the authors	ID3	
5	Data from 3D seismic interpretation verified by the authors	ID3	
6	Published 3D seismic data interpretation using trusted methods	ID3	
7	Firsthand mapping of 21,000+ horizontal wells	ID2	
8	Published 2D seismic data interpretation verified by the authors	ID2	Faults with moderate confidence (n = 73)
9	Published 2D seismic data interpretation using trusted methods	ID2	
10	Fault maps submitted to the Texas Railroad Commission developed using trusted methods	ID2	
11	Firsthand mapping controlled by 12,500+ vertical wells	ID1	
12	Published mapping of vertical wells verified by the authors	ID1	

by Zoback and Zoback (1989). It is convenient that $S_{H\,max}$ orientations and *relative* stress magnitudes typically do not change significantly with depth (e.g., Brudy *et al.*, 1997; Walsh and Zoback, 2016). Hence, the measurements shown in Figure 7 represent the stress field in the basin sediments as well as the crystalline basement below.

$S_{H\,max}$ orientations were measured using established methods, principally the mean azimuths of wellbore failure and fast shear-wave polarization, as described in detail by Boness and Zoback (2004) and Zoback (2007). About 18 of our new $S_{H\,max}$ orientations are from drilling-induced tensile fracture or borehole breakout azimuths measured using image logs in subvertical boreholes. Another three new $S_{H\,max}$ orientations are from inversions of microseismic focal mechanisms. Of the previously published $S_{H\,max}$ orientations, 26 are from Lund Snee and Zoback (2016), 13 are from the World Stress Map (Heidbach *et al.*, 2016), and the remainder were compiled from other published sources. Of the previously published $S_{H\,max}$ orientations, 28 are from borehole breakouts and drilling-induced tensile fractures, four are from earthquake focal mechanism inversions, and 13 are from fast shear-wave polarization directions measured using cross-dipole sonic logs.

An additional 11 new measurements were obtained from the mean orientations of aligned microseismic events defining hydraulic fractures observed during oil and gas operations. Because hydraulic fractures are planes that propagate in the direction of the maximum and intermediate principal stresses, viewing these features in map view indicates the orientation of $S_{H\,max}$ in normal- and strike-slip-faulting areas such as the FWB (in areas of reverse faulting, hydraulic fractures are horizontal). During reservoir stimulation, aligned groups of microseismic events produced by shear failure of small fractures typically surround the propagating hydrofrac, defining its geometry (Albright and Pearson, 1982). This technique for measuring $S_{H\,max}$ orientations and accompanying quality criteria were described by Lund Snee and Zoback (2018).

In addition to the new and previously published data, we modified metadata for $S_{H\,max}$ orientations that were originally published by Tingay *et al.* (2006) on the basis of previously unpublished information (R. Cornell, personal comm., 2017). Although this additional information was insufficient to upgrade any of their measurements to C quality or better (and hence insufficient to be used as constraints for FSP analysis and included in Fig. 7), the consistency among these measurements, and between these and higher-quality measurements, both here and in the Permian basin to the west (Lund Snee and Zoback, 2018), suggests that many might be reliable if more information was available. These and other D-quality data are included together with the higher-quality $S_{H\,max}$ orientations in Ⓔ Dataset S1.

Relative stress magnitudes are presented using the A_ϕ parameter as defined by

$$A_\phi = (n + 0.5) + (-1)^n(\phi - 0.5), \tag{1}$$

in which

$$\phi = \frac{S_2 - S_3}{S_1 - S_3}, \tag{2}$$

and where S_1, S_2, and S_3 represent the magnitudes of the maximum, intermediate, and minimum principal stresses, respectively (Simpson, 1997). The variable n is 0 for normal faulting, 1 for strike-slip faulting, and 2 for reverse faulting. The n-value is often inherently provided by most stress magnitude measurement techniques as these methods often determine the relative magnitudes of $S_{H\,max}$, $S_{h\,min}$, and S_v, which define the general faulting regime (see e.g., Zoback, 2007). A_ϕ measurements were obtained by several techniques, including precise constraints using focal mechanism stress inversions and approximate values estimated from interpretation of focal mechanisms, observations of active fault types during hydraulic-fracturing operations, and recent (Holocene) paleoseismic records (Madole, 1988; Crone and Luza, 1990). Here, we contribute four new A_ϕ values (Table 2), which supplement seven values previously reported in this area by Sone and Zoback (2014), Xu and Zoback (2015), Lund Snee and Zoback (2016), Kuang *et al.* (2017), and Quinones *et al.* (2018). As listed in Table 2, the new measurements are from formal inversions of microseismic focal mechanisms and interpretations of the faulting regime indicated by focal mechanisms and microseismic events defining active strike-slip faulting during reservoir stimulation. In their stress map of Texas, Lund Snee and Zoback (2016) included one very low A_ϕ value ($A_\phi = 0.18$) from measurements by Vermylen and Zoback (2011). We exclude this measurement because it probably results from viscous stress relaxation in the clay-rich Barnett Shale and hence does not reflect the conditions in stiffer rocks including the crystalline basement.

Using this updated stress map, we defined four zones of relatively constant stress conditions (Fig. 7), which are rectangular for simplicity and repeatability. Best estimates for $S_{H\,max}$ orientations were interpreted based on their range within each stress area, and taking into account regional trends from Lund Snee and Zoback (2016, 2018). Representative values of A_ϕ were assigned to each stress area values based on an interpolation between A_ϕ measurements. In general, the faulting regime transitions gradually from strike slip/normal in the northern and western parts of the FWB study area (stress areas 1 and 2), with A_ϕ values of 1.2 and 1.0, respectively, to normal faulting to the east and south (stress areas 3 and 4) with A_ϕ of 0.8 (Fig. 7). This trend is part of a broader regional transition from strike-slip/reverse faulting in southern Oklahoma to normal faulting in southern Texas (Lund Snee and Zoback, 2016). $S_{H\,max}$ is consistently approximately north-northeast–south-southwest across most of the FWB, with area means ranging from N038°E in stress area 1 to N025°E in stress area 3. We assign uncertainty

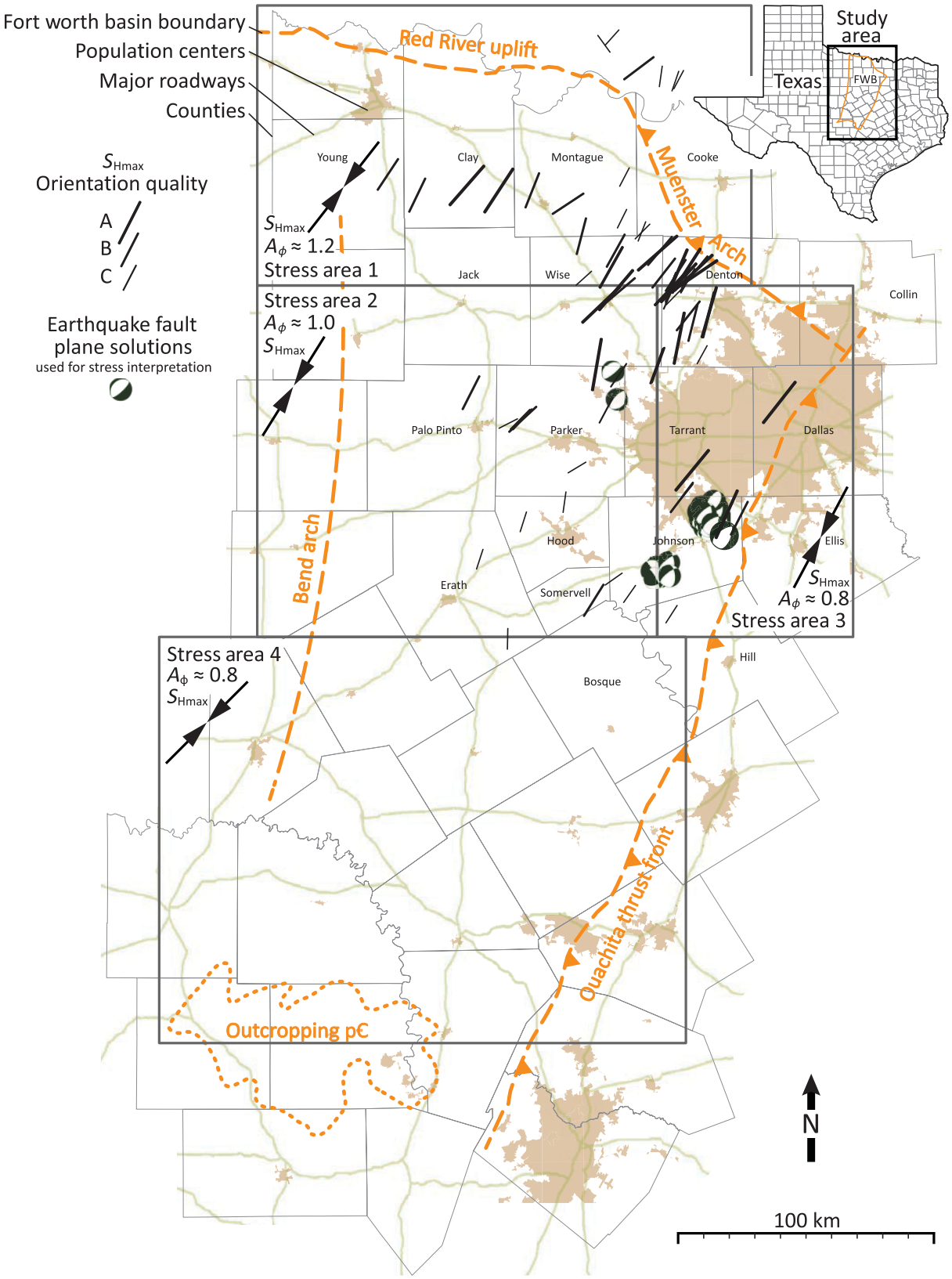

Figure 7. Map showing the outlines of four fault-slip potential (FSP) stress areas and the data used to constrain the mean $S_{H\,max}$ azimuth and A_ϕ value (faulting regime), as well as their uncertainty ranges used for FSP analysis. Stress data are from this study and Heidbach *et al.* (2016), Lund Snee and Zoback (2016), Alt and Zoback (2017), and Quinones *et al.* (2018). Area 4 lacks wellbore stress data, and therefore stress conditions were interpolated from data presented here and by Lund Snee and Zoback (2016). Earthquake locations and focal mechanisms are from Herrmann *et al.* (2011), Justinic *et al.* (2013), and Quinones *et al.* (2018).

Table 2
Measurements of Relative Principal Stress Magnitudes in the Fort Worth Basin, Reported Using the A_ϕ Parameter of Simpson (1997) Shown in Figures 7–9

Latitude (°)	Longitude (°)	A_ϕ	Point Type	Data Type	Source
33.39	−97.38	1.00	Interpreted	Aligned microseismic events (subsea faulting)	This study
33.20	−97.20	0.87	Precise	Formal focal mechanism inversion	This study
32.30	−97.37	0.90	Interpreted	Interpreted from focal mechanisms	This study
30.62	−96.44	0.75	Interpreted	Interpreted from microseismic focal mechanisms	This study
33.62	−98.29	1.25	Control	Interpolation guide point (no constraint)	This study
34.20	−100.15	1.25	Control	Interpolation guide point (no constraint)	This study
32.40	−97.42	0.81	Precise	Formal inversion of microseismic focal mechanisms	Kuang *et al.* (2017)
32.86	−96.91	0.435	Precise	Formal focal mechanism inversion	Quinones *et al.* (2018)
32.49	−97.15	0.493	Precise	Formal focal mechanism inversion	Quinones *et al.* (2018)
32.92	−100.83	1.20	Interpreted	Interpreted from focal mechanisms	Lund Snee and Zoback (2016)
34.54	−98.07	1.75	Interpreted	Paleoseismic	Crone and Luza (1990) and Madole (1988)
33.31	−97.32	1.20	Precise	*In situ*	Sone and Zoback (2014)
31.14	−101.19	0.822	Precise	*In situ*	Xu and Zoback (2015)

ranges to $S_{H\,max}$ for FSP analysis based on the range of measured orientations within each study area, and uncertainties for A_ϕ are based on its observed gradient when interpolated across each stress area. Although very little data are available directly within stress area 4, it is located within a clockwise west rotation of $S_{H\,max}$, from north-northeast–south-southwest in the northern FWB to approximately west–east in West Texas (Lund Snee and Zoback, 2016, 2018, this study). We estimate that $S_{H\,max}$ is oriented ∼N045°E in stress area 4, and we assign a broad ±20° uncertainty range based on the lower certainty for this estimate. Parameter values and uncertainties in each stress area for various geomechanical properties used for FSP analysis are given in Table 3. A tabulation of our assumption of the pore-pressure increase above hydrostatic in comparison to published information for the FWB is shown in Table 4.

FSP Method and Results

Pursuant to developing a comprehensive assessment of seismic hazard of an area influenced by pore-pressure change from SWD, it is vital to understand the sensitivity of known faults in their native preinjection state and with consideration of likely increases in pore pressure. We estimate the slip potential on faults using FSP v.1.07 (Walsh *et al.*, 2017), following the approaches of Walsh and Zoback (2016) and Lund Snee and Zoback (2018). As detailed by Walsh *et al.* (2017), FSP allows for screening-level analysis to identify faults that might be prone to slip; it does not calculate the actual probability that a fault will actually slip due to uncertainty determining a particular fault's position within its earthquake cycle, as well as heterogeneities in geometries, resolved stresses, pore pressure, and material properties at fine scales.

Specifically, FSP calculates the probability that planar fault segments will be critically stressed within the ambient stress field at a specified or modeled pore pressure. FSP uses a linearized Mohr–Coulomb failure criterion for faults within the specified stress field and pore-pressure conditions, with critically stressed conditions occurring when the ratio of resolved shear stress to normal stress reaches or exceeds the failure envelope. In practice, uncertainties are associated with all input parameters, including the fault strike and dip, ambient stress field, fault properties, and initial fluid pressure. Hence, we utilize the probabilistic geomechanics function in the FSP program, which applies Monte Carlo-type analysis to randomly sample values of each input parameter from specified, uniform uncertainty distributions (Table 3).

In this analysis, we do not hydrologically model the pressure changes associated with any known injection scenario. Instead, we estimate the FSP of two cases: a hydrostatic condition with no increase in pore fluid pressure (case 1), and a modest, uniform 1 MPa (145 pound per square inch [psi]) pore-pressure increase above hydrostatic (case 2). Case 1 enables us to estimate the distribution of FSP in the FWB before the onset of SWD, which we compare with results of case 2 indicating how the FSP would change if subjected to the pressure increase. We do not imply that the basin has experienced a uniform 1 MPa pore-pressure increase; we instead use this conservative value for case 2 to assess how the FSP of each 100 m fault segment sample *would* change due to that magnitude of increase. The case 2 pore-pressure increase is quite conservative when compared with other analyses of pressure increases in the FWB as described in previous work (compiled in Table 4). The hydrostatic gradient varies throughout the basin from 9.8 MPa/km (0.433 psi/ft) in the southwest to 11.1 MPa/km (0.491 psi/ft) in the northeast as a function of salinity (Texas Water Development Board [TWDB], 1972). The FSP program estimates absolute magnitudes of the two horizontal principal stresses ($S_{H\,max}$ and $S_{h\,min}$) from the provided A_ϕ values, coefficient of friction, and overburden stress gradient (S_v) in each stress area (Table 3), assuming that the crust is in a state of frictional failure equilibrium (Zoback *et al.*, 2002). We estimate that S_v is ∼26 MPa/km (1.15 psi/ft) based on our analysis of density logs throughout the study area.

We summarize the distribution of FSP for the entire FWB (Figs. 8 and 9), an inset area containing the studied

Table 3

Input Parameters Used for the Fault-Slip Potential (FSP) Analysis Shown in Figures 8–10

	FSP Inputs																			Stress Gradients		
Stress Area	Northwest Latitude (°)	Northwest Longitude (°)	Southeast Latitude (°)	Southeast Longitude (°)	$S_{H\,max}$ Azimuth (°)	$S_{H\,max}$ Azimuth Unc (°)	A_ϕ	A_ϕ Unc	Cohesion	Fault μ	Fault μ Unc	Reference Depth (m)	Initial P_p (psi/ft)	Initial P_p Unc (psi/ft)	P_p Inc (psi)	S_v (psi/ft)	S_v Unc (psi/ft)	Fault-Strike Unc (°)	Fault-Dip Unc (°)	S_V (MPa/km)	$S_{h\,max}$ (MPa/km)	Sh min (MPa/km)
1	34.20	−99.00	33.25	−97.00	38	20	1.18	0.30	0	0.7	0.05	3300	0.493	0.05	0, 145	1.15	0.05	5	10	26.01	28.46	14.86
2	33.25	−98.80	32.10	−97.40	32	16	1.00	0.22	0	0.7	0.05	2900	0.471	0.05	0, 145	1.15	0.05	5	10	26.01	26.01	14.20
3	33.25	−97.40	32.10	−96.40	25	15	0.80	0.21	0	0.7	0.05	3900	0.466	0.05	0, 145	1.15	0.05	5	10	26.01	23.65	14.20
4	32.10	−99.40	30.70	−97.20	45	20	0.82	0.15	0	0.7	0.05	2000	0.433	0.05	0, 145	1.15	0.05	5	10	26.01	23.89	14.20

Data used to calculate representative hydrostatic gradients were sourced from the Texas Water Development Board (1972). Inc, increase; Unc, uncertainty.

Table 4

Comparison of Our Assumption of a Pore-Pressure Increase of 1.0 MPa for the Case 2 FSP Analysis with Pore Pressures from Other Studies of the Fort Worth Basin and FSP Studies of Other Areas

		Stress Area 2		Stress Area 3							
		Azle		DFW Airport			Irving–Dallas		Venus		
Reference	Method/Source	Low Range (MPa)	High Range (MPa)	Low Range (MPa)	High Range (MPa)	Cleburne (MPa)	Low Range (MPa)	High Range (MPa)	Low Range (MPa)	High Range (MPa)	This and Other FSP Studies
Gono *et al.* (2015)	Simplistic fluid flow modeling			2.07	4.14	2.07					
Hornbach *et al.* (2015)	Simplistic fluid flow modeling	0.01	0.20								
Hornbach *et al.* (2016)	Cited measurements as per TX RRC								1.7	4.5	
Walsh and Zoback (2016)	Assumption based on cited studies										2.0 MPa
Scales *et al.* (2017)	Analysis of fall-off test data								0.9	4.8	
Chen *et al.* (2018)	Wellhead pressure matching	1.90	3.10								
Quinones *et al.* (2018)	Earthquake focal mechanisms	3.51	6.99				1.1	5.87	−0.23	4.31	
Lund Snee and Zoback (2018)	Assumption										0.4 MPa/km
Our case 2 analysis	assumption										1.0

TX RRC, Railroad Commission of Texas.

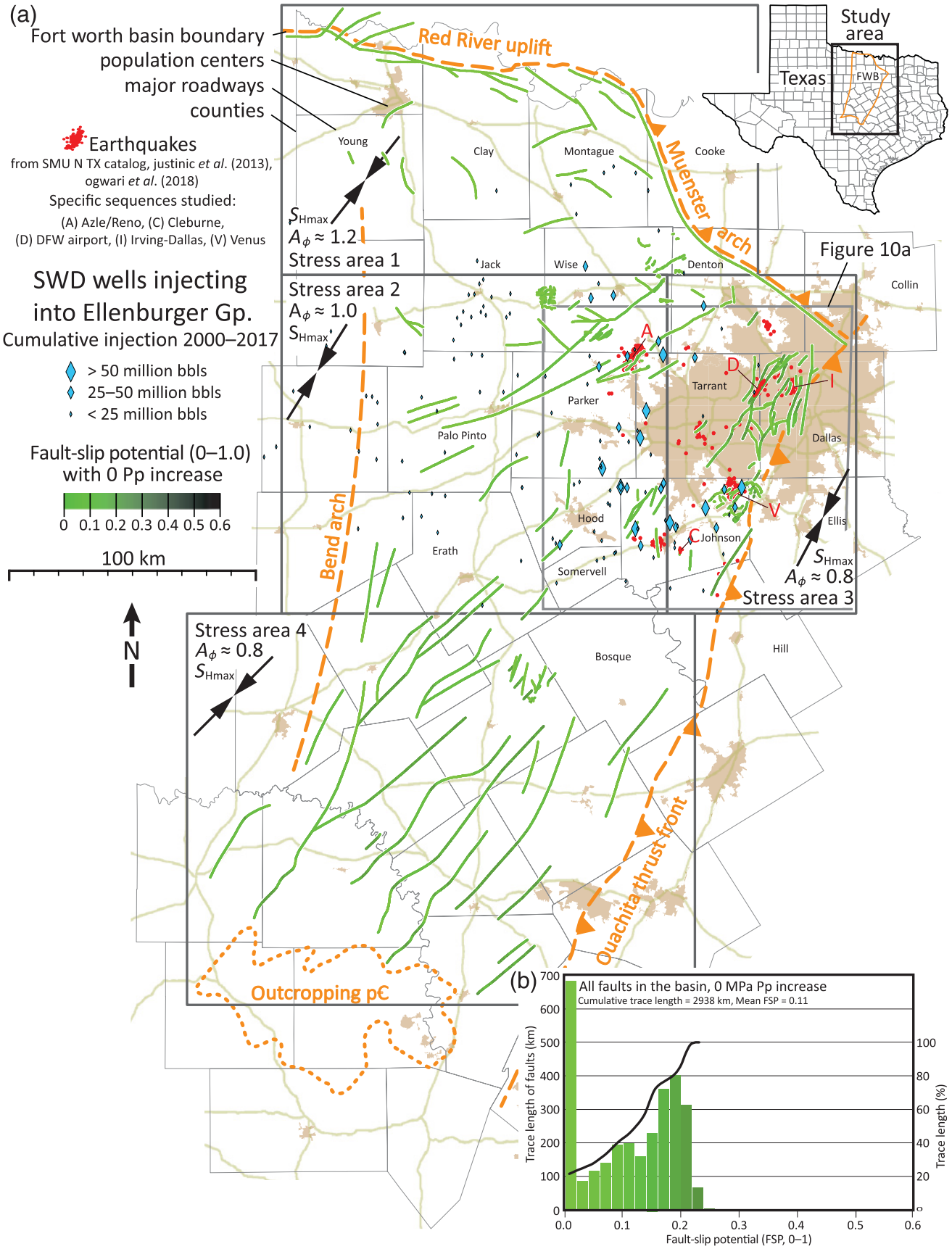

Figure 8. (a) Map of FSP in the Fort Worth basin for the case of hydrostatic pore-pressure conditions. (b) Distribution of FSP for the fault segments in (a). The possible range of FSP is 0–1.0.

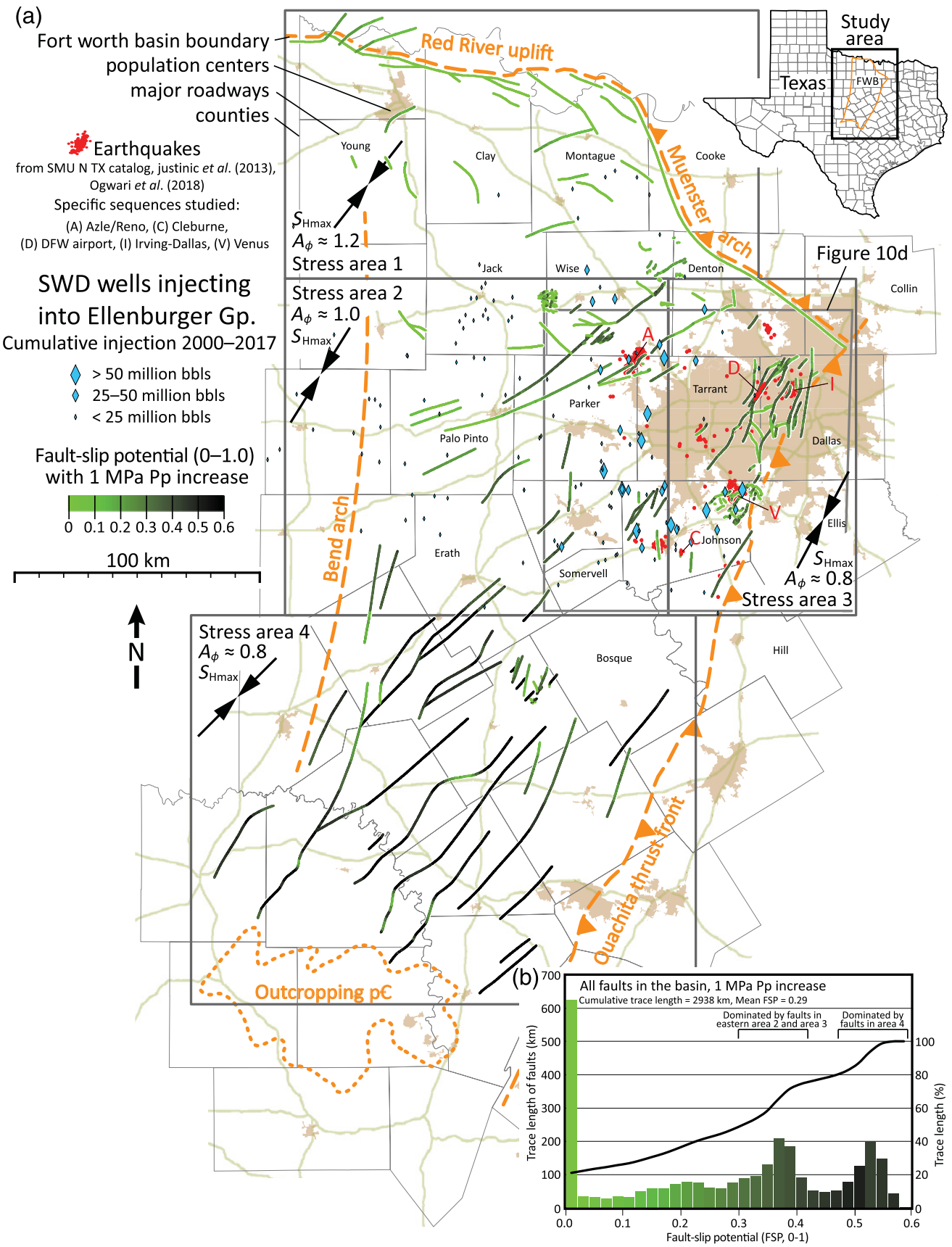

Figure 9. (a) Map of FSP in the Fort Worth basin for the case of 1 MPa increase in pore pressure. (b) Distribution of FSP for the fault segments in (a). The possible range of FSP is 0–1.0.

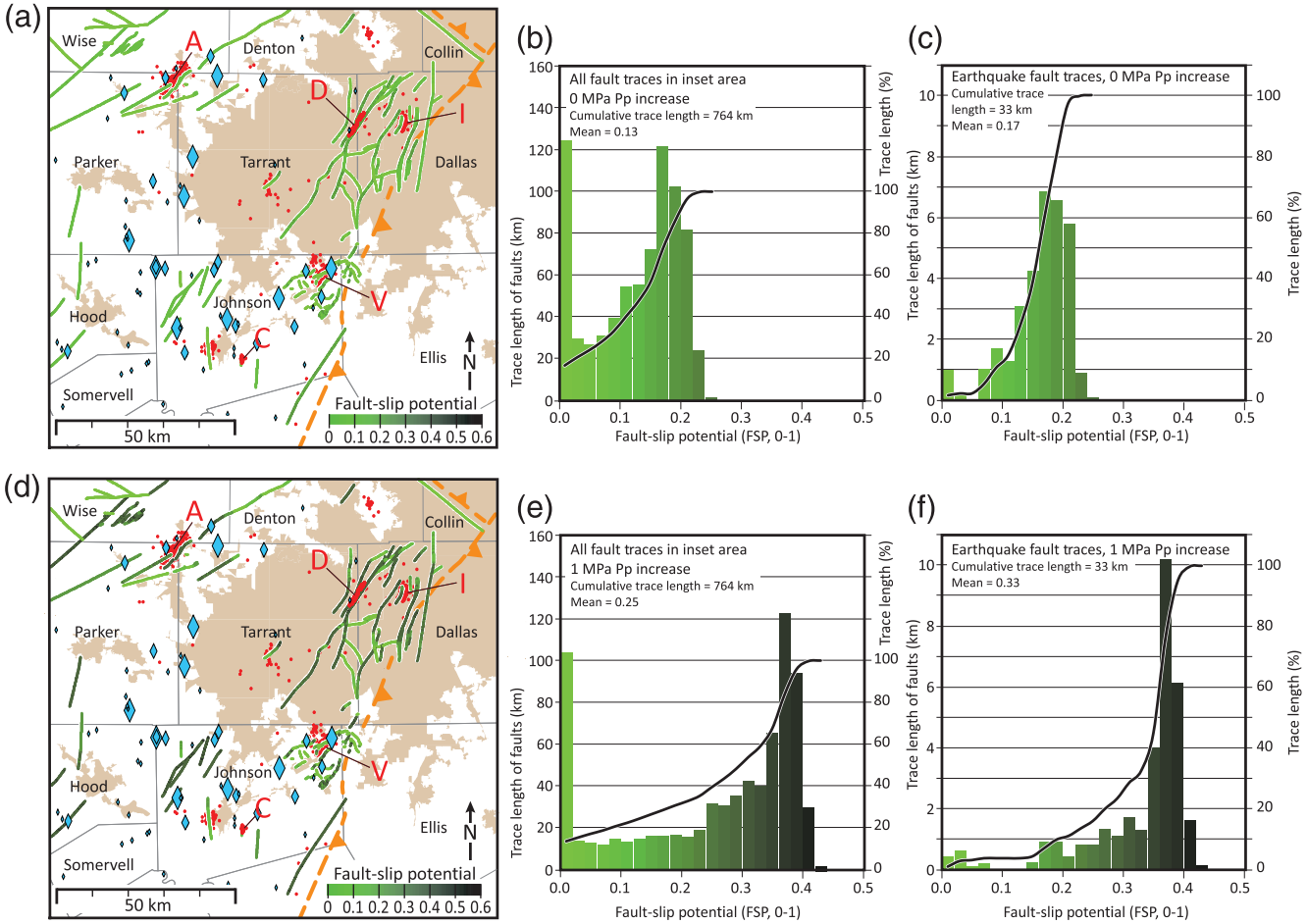

Figure 10. FSP maps and distributions of the inset areas indicated in Figures 8a and 9a containing the wells in the basin with largest cumulative injection volumes, earthquake sequences, and higher-confidence fault interpretation. (a) FSP map for the case of hydrostatic conditions; (b) FSP distribution for the fault segments in (a); (c) FSP distribution for the fault segments in (a) that have hosted earthquakes; (d) FSP map for the case of 1 MPa increase in pore pressure; (e) FSP distribution for the fault segments in (d); (f) FSP distribution for the fault segments in (d) that have hosted earthquakes. The possible range of FSP is 0–1.0.

earthquake sequences where we have greater confidence in our fault interpretation, and for the specific fault segments that hosted earthquakes (Fig. 10). FSP for all 2938 km of CTL in the FWB range for case 1 (hydrostatic) between 0.00 and 0.24, with a mean of 0.11 (Fig. 8a). As expected, due to the prevalence of normal faulting throughout, and especially the southern parts of the FWB, fault segments that strike subparallel to $S_{\mathrm{H\,max}}$ typically have higher FSP than fault segments with a greater angular divergence from $S_{\mathrm{H\,max}}$. In stress areas 1 and 2, where normal and strike-slip faulting are both active, faults subtending ~30° from $S_{\mathrm{H\,max}}$ also have higher FSP. Under this hydrostatic pore-pressure scenario, ~20% of the CTL has very low FSP (0.00–0.02) because they strike northwest (nearly perpendicular to $S_{\mathrm{H\,max}}$). These faults are mainly located in stress area 1. The remaining ~80% has an FSP distribution that is skewed to higher values (Fig. 8b). The FSP for the 764 km of CTL in the inset area for case 1 ranges 0.00–0.26 (Figs. 10a,b). The mean FSP is 0.13 and the distribution closely mirrors that of the entire FWB (Fig. 8b). The FSP of the 33 km of the CTL of fault segments that hosted the studied earthquake sequences has the same range and general skew as the whole inset area, with a mean of 0.17 (Fig. 10c).

For case 2 (1 MPa above hydrostatic pore pressure), the FSP range of 0.00–0.60 is much greater than that for case 1, as is its mean of 0.29 (Fig. 9a). Similar to case 1, an appreciable portion of the CTL (20%) has low FSP values between 0.00 and 0.20, indicating that many faults are extremely unlikely to slip at any increase in pore pressure. The remaining population is skewed toward higher FSP values, with a bimodal distribution centered near ~0.38 and ~0.54 (Fig. 9b). Fault segments with the highest FSP are mainly concentrated in stress area 4 where the overall population strikes dominantly northeast, subparallel to $S_{\mathrm{H\,max}}$ in that normal-faulting area. FSP is compounded in stress area 4 in part because that region has the shallowest depth to basement and fault traces, and lowest hydrostatic pore pressure so that, when increased by 1.0 MPa, it produces a large relative increase in FSP. The FSP for the inset area for case 2 ranges from 0.00 to 0.44, with a mean of 0.25 (Figs. 10d,e). The FSP

distribution within the inset is strongly skewed toward higher values, lacking the mode centered at 0.54 as compared to its counterpart in Figure 9b (which is dominated by the FSP of fault segments in stress area 4 as described earlier). The FSP for the earthquake fault segments in case 2 (Fig. 10f) also has the same range and general skew as the whole inset area (Fig. 10e), and a relatively high mean of 0.33.

Discussion

Faults in the FWB

Our new fault interpretation incorporates data from a range of publicly available and proprietary sources. Although we have been comprehensive, our interpretation is inherently incomplete with regard to fault identification and is uneven in its portrayal of fault density. Areas that benefit from the use of 3D seismic data, which provides the best capability to interpret small faults (ID3 in Fig. 1), reveal fault densities that are similar to what is observed in outcrops along the southwest flank of the basin. Hence, it is likely that the spatial density of faults at the length scale of 0.5 + km is as high in other areas of the basin as it is in areas ID3. Given that most of the known earthquake-producing faults are less than 10 km long (Fig. 6), their comprehensive characterization is best performed with 3D reflection seismic data. Cross sections across the basin (Fig. 2) illustrate that the faulting intensity (both closer spacing and greater offsets) appears to increase eastward toward the Ouachita thrust front. Although our interpretation control is highly variable spatially, this observation suggests that many of the northeast-striking faults that we observe could have originated during or after the Ouachita orogenic event, perhaps due to flexural stresses associated with overthrusting from the southeast. The geometry of faults observed in the new model poses a number of implications and new constraints for the tectonic history of the region, although it is outside the scope of the present study to address these issues.

Previous authors postulated that the ongoing Irving–Dallas sequence could have been induced by pore-pressure increases that traveled ≥30 km from areas of major SWD such as Johnson, Somervell, and Tarrant counties, perhaps channeled along major north-northeast-striking faults (Hornbach *et al.*, 2015). Aside from the new fault interpretation and FSP analysis on the causative structures, our study does not directly address those enigmatic earthquakes. Our fault interpretation does, however, document a system of north-northeast-striking faults that are connected by oblique segments in this area, all of high confidence, in addition to the faults and deformation associated with the north-northeast-trending Ouachita orogenic front (Fig. 1). Many of these north-northeast-striking faults have relatively high FSP, and critically stressed faults are often preferentially permeable (Barton *et al.*, 1995; Hennings *et al.*, 2012), but it is not known whether faults with elevated FSP might be able to preferentially transmit pore fluid pressure, especially over such long distances. The data and observations presented here can be used as inputs for hydrogeologic and geomechanical modeling to study the potential of long-distance inducement of fault reactivation in the FWB.

FSP

As expected for the dominantly normal-faulting conditions in the FWB, the highest FSP is observed on steeply dipping faults that strike north-northeast, parallel to $S_{H\,max}$. In northern areas with a strike-slip/normal stress state, FSP is also higher on faults subtending 30° from $S_{H\,max}$. The FSP values are relatively low across the entire basin for the ambient case with no increase in pore pressure (case 1 in Fig. 8). With an addition of 1 MPa of pore pressure (case 2 in Fig. 9), the FSP increases significantly, resulting in a near tripling of the mean (0.11 vs. 0.29). We note that the fault segments in stress area 4 drive this increase in FSP strongly for the reasons discussed previously. Focusing only on the inset area containing the population centers, injection wells, earthquake sequences, and higher-confidence fault interpretations, increasing the pore pressure by 1 MPa roughly doubles the mean FSP (Fig. 10b vs. 10e).

We can use the FSP values obtained for the 33 km of CTL for the faults that have recently hosted earthquakes as indicators of FSP that is associated with earthquake hazard in the FWB. For case 1, the hydrostatic scenario representing the time before the onset of SWD and induced seismicity, 90% of the seismogenic fault segments in the inset have FSP < 0.20 (Fig. 10c). We infer that this distribution of FSP reflects a collective geomechanical condition of fault stability in the FWB. However, with the addition of 1 MPa of pore pressure (case 2), 90% of the CTL for faults that have hosted earthquakes have FSP > 0.20 (Fig. 10f). Although this analysis cannot be used as a test of FSP magnitude that can be specifically linked to earthquakes in the FWB, the relatively modest increase in pore pressure of 1 MPa clearly drives the FSP much higher in this area and may be indicative of the change in conditions that would be conducive for fault reactivation and systemic instability. More importantly, the case 2 distribution of FSP for the fault segments in the inset, which have hosted earthquakes (Fig. 10f), is nearly identical to that of the overall population of 764 km of fault segments in the inset area with the exception of the 0.00–0.02 FSP mode in Figure 10e. From this, we infer that the overall population of faults in the inset is, in general, as sensitive to reactivation as the faults that produced earthquakes.

An obvious question is why earthquakes occurred only along such a limited length of faults (~33 km out of 764 km for the inset area and 2938 km for the entire basin) while there are so many sensitive faults in the basin that have not hosted earthquakes. Answering this question requires detailed and currently unknown information about the dynamic state of the faults, including where they are in their earthquake cycles and the degree of pore-pressure change they experienced. This research does not directly address these questions but our

interpretation of faults and FSP can be married with regional hydrogeologic modeling studies such as those by Gono *et al.* (2015), Hornbach *et al.* (2016), and Zhai and Shirzaei (2018) to quantitatively assess how increases in pore pressure and the distribution of sensitive faults spatiotemporally interact to elevate the earthquake hazard.

In addition, we observe that most recent earthquakes in the FWB have occurred on faults less than 8 km in length (Fig. 5). Because our fault interpretation is incomplete across the basin at that scale, it is likely that there are many more unidentified faults in the FWB, most of which are sensitive to reactivation.

Although it is clear that operators should avoid increasing the pore pressure near potentially active faults, we caution that FSP should not be used to fix a threshold between faults regarded as hazardous and stable, considering the uncertainties inherent in this analysis and the uncertainties about how far elevated fluid pressures might travel within high-permeability fault zones.

Implications for Further Hydrocarbon Development in the FWD and SWD

Approximately 20,000 wells were drilled in the FWB prior to 2018 and are responsible for almost 20 trillion cubic feet (TCF) of gas produced thus far and about 28 TCF to be ultimately recovered (Ikonnikova *et al.*, 2018). During this period, ~2 billion barrels of SWD occurred in the basin, reaching a peak rate of ~23 million barrels per month in 2011–2012 (Fig. 3). The rate of hydrocarbon development in the basin slowed significantly following the decline in oil and gas prices in 2014, as did the rate of SWD, and ultimately, the rate of seismicity. By the end of 2017, the monthly rate of injection across the basin (~9 MMbbls/mo) was roughly equal to the rate in 2007, prior to the onset of earthquakes (Fig. 3). This basinwide decrease has been followed by an overall decline in seismicity rate but, as noted earlier, the sequences active during the peak of injection have remained active, and new clusters have recently emerged (Quinones *et al.*, 2019). Injection rates across the basin remain elevated, with rates nearly four times those when injection accelerated in 2004. Injection has been concentrated in Johnson, Tarrant, and Parker counties (Hornbach *et al.*, 2016), near areas of continued seismicity. Estimates of the total technically recoverable resources in the basin are about 86 TCF out of 444 TCF of the original free gas in place (Ikonnikova *et al.*, 2014). It is estimated that 348 million barrels of shale-oil and natural gas liquids are also recoverable (Marra, 2018). Future rejuvenation of hydrocarbon development should be done with the understanding that the basin contains systems of faults, both interpreted and unknown, which are highly sensitive to pore-pressure changes. Throughout the central and southern parts of the basin, steeply dipping, north- to north-northeast-striking faults are a concern for both reactivation potential, and potentially, as enhanced pore-pressure conduits. In the northern areas, faults striking north to east-northeast may be susceptible to normal and strike-slip reactivation. Hazard assessment supporting SWD should be conducted with this understanding and should utilize the best possible data and methods for characterization.

Data and Resources

The fault interpretation was performed by integrating published data, publicly available data, well data as interpreted from the IHS Markit database under academic license, and fault data from proprietary 3D reflection seismic data as interpreted or verified firsthand by the authors. Faults for area ID3a (Fig. 1) come from direct interpretation of the Boonsville 3D Seismic Data Set that can be obtained at https://store.beg.utexas.edu/cd-rom-sets/1311-sw0007.html (last accessed November 2018). Faults for areas ID3b and ID3c come from fault data provided by petroleum operators using proprietary seismic data. These interpretations were verified firsthand by P. H. H. for ID3b and by P. H. H. and E. H. for ID3c. The interpretation of faults in the eastern portion of area ID2 benefitted from data publicly available from the Railroad Commission of Texas Hearing Docket 09-0296411. Data for the stress interpretation of the FWB added for this study were provided by petroleum operators using proprietary well and microseismic data as verified by J.-E. L. S. A tabulation of this data is provided in the Ⓔ Table S1 (available in the supplemental content to this article). Geographic Information Systems (GIS) shapefiles of the fault traces used in the study are available in Ⓔ Dataset S1. U.S. Geological Survey (USGS) Advanced National Seismic System Comprehensive Catalog (ComCat) is available https://earthquake.usgs.gov/earthquakes/search/ (last accessed January 2019).

Acknowledgments

The authors thank Dana Jurick, Alan Morris, Scott Tinker, Cezar Trifu, Editor-in-Chief Thomas Pratt, and two anonymous reviewers for suggestions that greatly improved the article. The authors thank ConocoPhillips, MicroSeismic, Inc., and Pioneer Natural Resources for access to new stress data, and XTO and ConocoPhillips for access to proprietary fault information from 3D reflection seismic data. The authors thank XTO and ExxonMobil for support in fault-slip potential (FSP) software development. The authors thank IHS Markit for access to well databases and Petra software, Schlumberger for access to the Petrel E&P Software Platform, Midland Valley for access to Move software, and Badleys for access to T7 software. This work was supported by The State of Texas through the University of Texas Bureau of Economic Geology the Texas Seismologic Network (TexNet) Seismic Monitoring and Research Project (P. H. H., J. L. O., R. D., H. R. D.), the industrial affiliates of the Center for Integrated Seismicity Research (CISR; P. H. H.), and the industrial affiliates of the Stanford Center for Induced and Triggered Seismicity (SCITS; J.-E. L. S., M. D. Z.).

References

Albright, J. N., and C. F. Pearson (1982). Acoustic emissions as a tool for hydraulic fracture location: Experience at the Fenton Hill hot dry rock site, *Soc. Petrol. Eng. J.* **22,** no. 04, 523–530, doi: 10.2118/9509-PA.

Alsalem, O. B., M. Fan, and X. Xie (2017). Late Paleozoic subsidence and burial history of the Fort Worth basin, *AAPG Bulletin* **101,** no. 11, 1813–1833, doi: 10.1306/01251716016.

Alt, R. C., and M. D. Zoback (2017). In situ stress and active faulting in Oklahoma, *Bull. Seismol. Soc. Am.* **107,** no. 1, 216, doi: 10.1785/0120160156.

Barnes, V. E., and P. R. Rose (1981). *Geologic Atlas of Texas, Llano Sheet (GA0020D, Scale 1:250,000)*, The University of Texas at Austin, Bureau of Economic Geology, Austin, Texas.

Barton, C. A., M. D. Zoback, and D. Moos (1995). Fluid flow along potentially active faults in crystalline rock, *Geology* **23,** no. 8, 683–686, doi: 10.1130/0091-7613(1995)023<0683:FFAPAF>2.3.CO;2.

Belforte, A. S. (1971). Pre-Canyon structural geology of the southern end of the Fort Worth basin, Central Texas, *Master's Thesis*, The University of Texas at Austin, Austin, Texas.

Boness, N. L., and M. D. Zoback (2004). Stress-induced seismic velocity anisotropy and physical properties in the SAFOD Pilot Hole in Parkfield, CA, *Geophys. Res. Lett.* **31,** no. 15, 15–18, doi: 10.1029/2003GL019020.

Brudy, M., M. D. Zoback, K. Fuchs, F. Rummel, and J. Baumgärtner (1997). Estimation of the complete stress tensor to 8 km depth in the KTB scientific drill holes: Implications for crustal strength, *J. Geophys. Res.* **102,** no. B8, 18,453–18,475, doi: 10.1029/96JB02942.

Chen, R., X. Xua, C. Yao, A. Datta-Gupta, and M. King (2018). Coupled fluid flow and geomechanical modeling of seismicity in the Azle area north Texas, *SPE Annual Technical Conference and Exhibition*, Dallas, Texas, 24–26 September, doi: 10.2118/191623-MS.

Crone, A. J., and K. V. Luza (1990). Style and timing of Holocene surface faulting on the Meers fault, southwestern Oklahoma, *Geol. Soc. Am. Bull.* **102,** no. 1, 1–17, doi: 10.1130/0016-7606(1990)102<0001:SATOHS>2.3.CO;2.

DeShon, H. R., C. T. Hayward, P. O. Ogwari, L. Quinones, O. Sufri, B. Stump, and M. B. Magnani (2018). Summary of the North Texas Earthquake Study Seismic Networks, 2013-2018, *Seismol. Res. Lett.* **90,** no. 1, 387–394, doi: 10.1785/0220180269.

Eastman, H. S., and T. Murin (2016). Geologic characterization of Johnson County, Texas, *NETL Technical Report Series (NETL-TRS-17-2016)*, U.S. Department of Energy, National Energy Technology Laboratory, Morgantown, West Virginia.

Elebiju, O. O., G. R. Keller, and K. J. Marfurt (2010). Investigation of links between Precambrian basement structure and Paleozoic strata in the Fort Worth basin, Texas, U.S.A., using high-resolution aeromagnetic (HRAM) data and seismic attributes, *Geophysics* **75,** no. 4, B157–B168, doi: 10.1190/1.3435939.

Ellsworth, W. L. (2013). Injection-induced earthquakes, *Science* **341,** no. 6142, 1225942, doi: 10.1126/science.1225942.

Ewing, T. (1991). *The Tectonic Framework of Texas: Text to Accompany the Tectonic Map of Texas*, Bureau of Economic Geology the University of Texas at Austin, Austin, Texas, retrieved from http://www.worldcat.org/title/tectonic-framework-of-texas-text-to-accompany-the-tectonic-map-of-texas/oclc/24400900 (last accessed November 2018).

Flawn, P. T., A. Goldstein Jr., P. B. King, and C. E. Weaver (1961). *The Ouachita System*, Bureau of Economic Geology, University of Texas, Austin, Texas, Publications 6120, 401 p.

Frohlich, C. (2012). Two-year survey comparing earthquake activity and injection-well locations in the Barnett Shale, Texas, *Proc. Natl. Acad. Sci. Unit. States Am.* **109,** no. 35, 13,934–13,938, doi: 10.1073/pnas.1207728109.

Frohlich, C., H. DeShon, B. Stump, C. Hayward, M. Hornbach, and J. I. Walter (2016). A historical review of induced earthquakes in Texas, *Seismol. Res. Lett.* **87,** no. 4, 1022–1038, doi: 10.1785/0220160016.

Frohlich, C., C. Hayward, B. Stump, and E. Potter (2011). The Dallas-Fort Worth earthquake sequence: October 2008 through May 2009, *Bull. Seismol. Soc. Am.* **101,** no. 1, 327–340, doi: 10.1785/0120100131.

Frohlich, C., E. Potter, C. Hayward, and B. Stump (2010). Dallas-Fort Worth earthquakes coincident with activity associated with natural gas production, *The Leading Edge* **29,** no. 3, 270, doi: 10.1190/1.3353720.

George, M. C. (2016). The Muenster uplift of North Texas: The easternmost expression of the Pennsylvanian ancestral rockies, *Master's Thesis*, The University of Texas at Dallas, Dallas, Texas.

Gono, V., J. E. Olson, and J. F. Gale (2015). Understanding the correlation between induced seismicity and wastewater injection in the Fort Worth basin, *49th US Rock Mechanics/Geomechanics Symposium*, American Rock Mechanics Assoc., San Francisco, California, 28 June–1 July 2015, 15–00419.

Hardage, B. A., D. L. Carr, D. E. Lancaster, J. L. Simmons, R. Y. Elphick, V. M. Pendleton, and R. A. Johns (1996). 3-D seismic evidence of the effects of carbonate karst collapse on overlying clastic stratigraphy and reservoir compartmentalization, *Geophysics* **61,** no. 5, 1336, doi: 10.1190/1.1444057.

Heidbach, O., M. Rajabi, K. Reiter, M. Ziegler, and W. Team (2016). *World Stress Map 2016*, GFZ Data Services, doi: 10.5880/WSM.2016.001.

Hennings, P., P. Allwardt, P. Paul, C. Zahm, R. Reid Jr., H. Alley, R. Kirschner, B. Lee, and E. Hough (2012). Relationship between fractures, fault zones, stress, and reservoir productivity in the Suban gas field, Sumatra, Indonesia, *AAPG Bulletin* **96,** no. 4, doi: 10.1306/08161109084.

Hentz, T. F., W. A. Ambrose, and D. L. Carr (2012). Reservoir systems of the Pennsylvanian lower Atoka Group (Bend Conglomerate), northern Fort Worth basin, Texas: High-resolution fades distribution, structural controls on sedimentation, and production trends, *AAPG Bulletin* **96,** no. 7, 1301–1332, doi: 10.1306/10041111078.

Herrmann, R. B., H. Benz, and C. J. Ammon (2011). Monitoring the earthquake source process in North America, *Bull. Seismol. Soc. Am.* **101,** no. 6, 2609, doi: 10.1785/0120110095.

Hornbach, M. J., H. R. Deshon, W. L. Ellsworth, B. W. Stump, C. Hayward, C. Frohlich, H. R. Oldham, J. E. Olson, M. B. Magnani, C. Brokaw, *et al.* (2015). Causal factors for seismicity near Azle, Texas, *Nat. Comm.* **6,** Article Number 6728, doi: 10.1038/ncomms7728.

Hornbach, M. J., M. Jones, M. Scales, H. R. DeShon, M. B. Magnani, C. Frohlich, B. Stump, C. Hayward, and M. Layton (2016). Ellenburger wastewater injection and seismicity in North Texas, *Phys. Earth Planet. In.* **261,** 54–68, doi: 10.1016/j.pepi.2016.06.012.

Howe, A. M. (2012). Analysis of the Cleburne earthquake sequence from June 2009 to June 2010, *Master's Thesis*, Southern Methodist University, Dallas, Texas.

Huang, Y., W. L. Ellsworth, and G. C. Beroza (2017). Stress drops of induced and tectonic earthquakes in the central United States are indistinguishable, *Sci. Adv.* **3,** no. 8, e1700772, doi: 10.1126/sciadv.1700772.

Ikonnikova, S., J. Browning, S. C. Horvath, and S. Tinker (2014). Well recovery, drainage area, and future drill-well inventory: Empirical study of the Barnett Shale gas play, *SPE Reserv. Eval. Eng.* **17,** no. 04, 484–496, doi: 10.2118/171552-PA.

Ikonnikova, S., K. Smye, J. Browning, and F. Male (2018). Update and enhancement of shale gas outlooks, available at https://www.osti.gov/biblio/1479289 (last accessed November 2018).

Janská, E., and L. Eisner (2012). Ongoing seismicity in the Dallas-Fort Worth area, *The Leading Edge* **31,** no. 12, doi: 10.1190/tle31121462.1.

Justinic, A. H., B. Stump, C. Hayward, and C. Frohlich (2013). Analysis of the Cleburne, Texas, earthquake sequence from June 2009 to June 2010, *Bull. Seismol. Soc. Am.* **103,** no. 6, 3083–3093, doi: 10.1785/0120120336.

Khatiwada, M., G. R. Keller, and K. J. Marfurt (2013). A window into the Proterozoic: Integrating 3D seismic, gravity, and magnetic data to image subbasement structures in the southeast Fort Worth basin, *Interpretation* **1,** no. 2, doi: 10.1190/INT-2013-0041.1.

Kier, R. S., L. F. Brown Jr., P. Hardwood, and V. E. Barnes (1976). *Geologic Atlas of Texas, Brownwood Sheet (GA0008, Scale 1:250,000)*, The University of Texas at Austin, Bureau of Economic Geology, Austin, Texas.

Krantz, B., and T. G. Neely (2016). Subsurface structural interpretation: The significance of 3-D structural frameworks, in *3-D Structural Interpretation: Earth, Mind, and Machine*, AAPG Memoir, Vol. 111**,** 91–109, doi: 10.1306/13561988M1113181.

Kuang, W., M. Zoback, and J. Zhang (2017). Estimating geomechanical parameters from microseismic plane focal mechanisms recorded during multistage hydraulic fracturing *Geophysics* **82,** no. 1, doi: 10.1190/geo2015-0691.1.

Langenbruch, C., and M. D. Zoback (2016). How will induced seismicity in Oklahoma respond to decreased saltwater injection rates? *Sci. Adv.* **2,** no. 11, e1601542, doi: 10.1126/sciadv.1601542.

Leary, R. J., P. Umhoefer, M. E. Smith, and N. Riggs (2017). A three-sided orogen: A new tectonic model for Ancestral Rocky Mountain uplift and basin development, *Geology* **45,** no. 8, 735–738, doi: 10.1130/G39041.1.

Lund Snee, J.-E., and M. D. Zoback (2016). State of stress in Texas: Implications for induced seismicity, *Geophys. Res. Lett.* **43,** no. 19, 10,208–10,214, doi: 10.1002/2016GL070974.

Lund Snee, J.-E., and M. D. Zoback (2018). State of stress in the Permian basin, Texas and New Mexico: Implications for induced seismicity, *The Leading Edge* 810–819, doi: 10.1190/tle37020127.1.

Madole, R. F. (1988). Stratigraphic evidence of Holocene faulting in the mid-continent: The Meers fault, southwestern Oklahoma, *Geol. Soc. Am. Bull.* **100,** no. 3, 392–401, doi: 10.1130/0016-7606(1988)100<0392:SEOHFI>2.3.CO;2.

Magnani, M. B., M. L. Blanpied, H. R. DeShon, and M. J. Hornbach (2017). Discriminating between natural versus induced seismicity from long-term deformation history of intraplate faults, *Sci. Adv.* **3,** no. 11, e1701593, doi: 10.1126/sciadv.1701593.

Marra, K. R. (2018). 2015 US Geological Survey assessment of undiscovered shale-gas and shale-oil resources of the Mississippian Barnett Shale, Bend arch-Fort Worth basin, Texas, *AAPG Bulletin* **102,** no. 07, 1299–1321, doi: 10.1306/0810171622017164.

McDonnell, A., R. G. Loucks, and T. Dooley (2007). Quantifying the origin and geometry of circular sag structures in northern Fort Worth basin, Texas: Paleocave collapse, pull-apart fault systems, or hydrothermal alteration? *AAPG Bulletin* **91,** no. 9, 1295–1318, doi: 10.1306/05170706086.

Ogwari, P. O., H. R. DeShon, and M. J. Hornbach (2018). The Dallas-Fort Worth Airport earthquake sequence: Seismicity beyond injection period, *J. Geophys. Res.* **123,** no. 1, 553–563, doi: 10.1002/2017JB015003.

Patterson, A. A. (2010). Structural geology and hydrocarbon production, Barnett Shale (Mississippian), Fort Worth basin, northwestern Johnson County, Texas, *Master's Thesis*, Texas Christian University, Fort Worth, Texas.

Pollastro, R. M., D. M. Jarvie, R. J. Hill, and C. W. Adams (2007). Geologic framework of the Mississippian Barnett Shale, Barnett-Paleozoic total petroleum system, Bend arch-Fort Worth basin, Texas, *AAPG Bulletin* **91,** no. 4, 405–436, doi: 10.1306/10300606008.

Poole, F. G., W. J. Perry, R. J. Madrid, and R. Amaya-Martínez, (2005). Tectonic synthesis of the Ouachita-Marathon-Sonora orogenic margin of southern Laurentia: Stratigraphic and structural implications for timing of deformational events and plate-tectonic model, in *Special Paper 393: The Mojave-Sonora Megashear Hypothesis: Development, Assessment, and Alternatives*, Vol. 393**,** Geological Society of America, 543–596, doi: 10.1130/0-8137-2393-0.543.

Quinones, L. A., H. R. DeShon, S.-J. Jeong, P. Ogwari, M. M. Scales, and K. B. Kwong (2019). Tracking induced earthquakes in the Fort Worth basin: A summary of the 2008-2018 North Texas earthquake study catalog, *Bull. Seismol. Soc. Am.* doi: 10.1785/0120190057.

Quinones, L. A., H. R. DeShon, M. B. Magnani, and C. Frohlich (2018). Stress Orientations in the Fort Worth basin, Texas, determined from earthquake focal mechanisms, *Bull. Seismol. Soc. Am.* **108,** no. 3A, 1124–1132, doi: 10.1785/0120170337.

Reiter, D., M. Leidig, S.-H. Yoo, and K. Mayeda (2012). Source characteristics of seismicity associated with underground wastewater disposal: A case study from the 2008 Dallas-Fort Worth earthquake sequence, *The Leading Edge* **31,** no. 12, 1454, doi: 10.1190/tle31121454.1.

Savvaidis, A., B. Young, D.-G. Huang, and A. Lomax (2019). TexNet: A statewide seismological network in Texas, *Seismol. Res. Lett.* doi: 10.1785/0220180350.

Scales, M. M., H. R. DeShon, M. B. Magnani, J. I. Walter, L. Quinones, T. L. Pratt, and M. J. Hornbach (2017). A decade of induced slip on the causative fault of the 2015 M_w 4.0 Venus earthquake, northeast Johnson County, Texas, *J. Geophys. Res.* **122,** no. 10, 7879–7894, doi: 10.1002/2017JB014460.

Simpson, R. W. (1997). Quantifying Anderson's fault types, *J. Geophys. Res.* **102,** no. B8, doi: 10.1029/97JB01274.

Sone, H., and M. D. Zoback (2014). Viscous relaxation model for predicting least principal stress magnitudes in sedimentary rocks, *J. Petrol. Sci. Eng.* **124,** 416–431, doi: 10.1016/j.petrol.2014.09.022.

Sullivan, E. C., K. J. Marfurt, A. Lacazette, and M. Ammerman (2006). Application of new seismic attributes to collapse chimneys in the Fort Worth Basin, *Geophysics* **71,** no. 4, doi: 10.1190/1.2216189.

Texas Water Development Board (1972). A survey of the subsurface saline water of Texas, *Texas Water Development Board Report 157*, Vol. 1**,** available at http://www.twdb.texas.gov/publications/reports/numbered_reports/doc/R157/report157.asp.

Thomas, W. A. (2004). Genetic relationship of rift-stage crustal structure, terrane accretion, and foreland tectonics along the southern Appalachian-Ouachita orogen, *J. Geodyn.* **37,** 549–563, doi: 10.1016/j.jog.2004.02.020.

Thompson, D. M. (1982). Atoka Group (Lower to Middle Pennsylvanian), northern Fort Worth basin, Texas: Terrigenous deposition systems, diagenesis, and reservoir distribution and quality, *Report of Investigations (No. 125)*, The University of Texas at Austin, Bureau of Economic Geology, Austin, Texas.

Tingay, M. R. P., B. Muller, J. Reinecker, and O. Heidbach (2006). State and origin of the present-day stress field in sedimentary basins: New results from the World Stress Map project, paper presented at the *41st U.S. Symposium on Rock Mechanics*, American Rock Mechanics Association, Golden, Colorado, 17–21 June.

Underground Injection Control National Technical Workgroup (2015). *Minimizing and Managing Potential Impacts of Injection-Induced Seismicity from Class II Disposal Wells: Practical Approaches: February 2015*, U.S. Environmental Protection Agency, Washington, D.C.

Vermylen, J., and M. D. Zoback (2011). Hydraulic fracturing, microseismic magnitudes, and stress evolution in the Barnett Shale, Texas, USA, *SPE Hydraulic Fracturing Technology Conference*, Society of Petroleum Engineers, SPE 140507, doi: 10.2118/140507-MS.

Viele, G. W., and W. A. Thomas (1989). Tectonic synthesis of the Ouachita orogenic belt, in *The Appalachian-Ouachita Orogen in the United States, Geology of North America*, R. D. Hatcher, W. A. Thomas, and G. W. Viele (Editors), Vol. F-2, The Geological Society of America, Boulder, Colorado, 695–728, available at http://rock.geosociety.org/Store/detail.aspx?id=DNAGGNAF2 (last accessed June 2019).

Walper, J. L. (1982). Plate tectonic evolution of the Fort Worth basin, *Petroleum Geology of the Fort Worth Basin and Bend Arch Area*, 237–253, retrieved from http://archives.datapages.com/data/dgs/009/009001/237_dgs0090237.htm (last accessed June 2019).

Walsh, F. R., and M. D. Zoback (2015). Oklahoma's recent earthquakes and saltwater disposal, *Sci. Adv.* **1,** no. 5, doi: 10.1126/sciadv.1500195.

Walsh, F. R., and M. D. Zoback (2016). Probabilistic assessment of potential fault slip related to injection induced earthquakes: Application to north-central Oklahoma, USA, *Geology* **44,** no. 12, 991–994, doi: 10.1130/G38275.1.

Walsh, F. R. I., M. D. Zoback, D. Pais, M. Weingartern, and T. Tyrell (2017). *FSP 1.0: A Program for Probabilistic Estimation of Fault Slip Potential Resulting from Fluid Injection*, available at https://scits.stanford.edu/software (last accessed November 2018).

Weingarten, M., S. Ge, J. W. Godt, B. A. Bekins, and J. L. Rubinstein (2015). High-rate injection is associated with the increase in U.S. mid-continent seismicity, *Science* **348,** no. 6241, doi: 10.1126/science.aab1345.

Xu, S., and M. D. Zoback (2015). Analysis of stress variations with depth in the Permian basin Spraberry/Dean/Wolfcamp Shale, paper presented at the *49th U.S. Rock Mechanics/Geomechanics Symposium*, American Rock Mechanics Association, San Francisco, California, 28 June–1 July 2015.

Zhai, G., and M. Shirzaei (2018). Fluid injection and time-dependent seismic hazard in the Barnett Shale, Texas, *Geophys. Res. Lett.* **45,** no. 10, doi: 10.1029/2018GL077696.

Zhang, Y., M. Person, J. Rupp, K. Ellett, M. A. Celia, C. W. Gable, B. Bowen, J. Evans, K. Bandilla, P. Mozley, *et al.* (2013). Hydrogeologic controls on induced seismicity in crystalline basement rocks due to fluid injection into basal reservoirs, *Groundwater* **51,** no. 4, doi: 10.1111/gwat.12071.

Zoback, M. D. (2007). *Reservoir Geomechanics*, Cambridge University Press, New York, New York, doi: 10.1017/CBO9780511586477.

Zoback, M. D. (2012). Managing the seismic risk posed by wastewater disposal, *Earth* **57,** no. 4, 38.

Zoback, M. D., J. Townend, and B. Grollimund (2002). Steady-state failure equilibrium and deformation of intraplate lithosphere, *Int. Geol. Rev.* **44,** no. 5, 383–401, doi: 10.2747/0020-6814.44.5.383.

Zoback, M. L., and M. D. Zoback (1989). Tectonic stress field of the continental United States, in *Geophysical Framework of the Continental United States*, L. C. Pakiser and W. D. Mooney (Editors), Geological Society of America Memoirs, Vol. 172, 523–540, doi: 10.1130/MEM172-p523.

Peter H. Hennings
Johnathon L. Osmond
Robin Dommisse
Elizabeth Horne
Casee Lemons
Bureau of Economic Geology
Jackson School of Geosciences
The University of Texas at Austin
PO Box X, University Station
Austin, Texas 78713-8924 U.S.A.
peter.hennings@beg.utexas.edu

Jens-Erik Lund Snee
Mark D. Zoback
Department of Geophysics
397 Panama Mall
Mitchell Building, 3rd Floor
Stanford University
Stanford, California 94305-2215 U.S.A.

Heather R. DeShon
Roy M. Huffington Department of Earth Sciences
Southern Methodist University
P.O. Box 750395
Dallas, Texas 75275-0395 U.S.A.

Manuscript received 30 January 2019;
Published Online 16 July 2019